DOT/FAA/AR-03/76

Office of Aviation Research
Washington, D.C. 20591

Assessment, Development, and Validation of Computational Fracture Mechanics Methodologies and Tools for Shot-Peened Materials Used in Rotorcraft Principal Structural Elements

July 2004

Final Report

This document is available to the U.S. public through the National Technical Information Service (NTIS), Springfield, Virginia 22161.

U.S. Department of Transportation
Federal Aviation Administration

NOTICE

This document is disseminated under the sponsorship of the U.S. Department of Transportation in the interest of information exchange. The United States Government assumes no liability for the contents or use thereof. The United States Government does not endorse products or manufacturers. Trade or manufacturer's names appear herein solely because they are considered essential to the objective of this report. This document does not constitute FAA certification policy. Consult your local FAA aircraft certification office as to its use.

This report is available at the Federal Aviation Administration William J. Hughes Technical Center’s Full-Text Technical Reports page: actlibrary.tc.faa.gov in Adobe Acrobat portable document format (PDF).

Technical Report Documentation Page

1. Report No. DOT/FAA/AR-03/76	2. Government Accession No.	3. Recipient's Catalog No.

4. Title and Subtitle ASSESSMENT, DEVELOPMENT, AND VALIDATION OF COMPUTATIONAL FRACTURE MECHANICS METHODOLOGIES AND TOOLS FOR SHOT-PEENED MATERIALS USED IN ROTORCRAFT PRINCIPAL STRUCTURAL ELEMENTS	5. Report Date July 2004
	6. Performing Organization Code
7. Author(s) S. Shen, Z. D. Han, C. A. Herrera, and S. N. Atluri	8. Performing Organization Report No.
9. Performing Organization Name and Address Center for Aerospace Research & Education 5251 California Avenue, Suite 140 University of California at Irvine Irvine, CA 92612	10. Work Unit No. (TRAIS)
	11. Contracts or Grant No. DTFA03-01-C00036
12. Sponsoring Agency Name and Address U.S. Department of Transportation Federal Aviation Administration Office of Aviation Research Washington, DC 20591	13. Type of Report and Period Covered Final Report
	14. Sponsoring Agency Code ASW-112

15. Supplementary Notes

The FAA William J. Hughes Technical Center COTR for this project was Dy Le.

16. Abstract

This report describes an analytical model that simulates the shot-peening process and estimates the residual stress field in the surface layer. A numerical approach for the prediction of crack growth rates for cracks in compressive stress fields was implemented in AGILE 3D. AGILE 3D is an accurate and efficient tool for predicting nonplanar three-dimensional (3D) fatigue crack growth in structural components. The results of validation of AGILE 3D for predicting 3D fatigue growth, compared to the University of Washington test data, were very good. The effect of shot peening on crack growth rates of various materials is investigated numerically by means of AGILE 3D. Various fatigue crack growth models, including plastic strip model and plastic zone model in the presence of residual stresses and plasticity, are discussed.

17. Key Words Shot peened, FEAM, AGILE 3D, Fatigue, Plastic strip model, Plastic zone model, Residual stress	18. Distribution Statement This document is available to the public through the National Technical Information Service (NTIS), Springfield, Virginia 22161.

19. Security Classif. (of this report) Unclassified	20. Security Classif. (of this page) Unclassified	21. No. of Pages 79	22. Price

Form DOT F 1700.7 (8-72) Reproduction of completed page authorized

ACKNOWLEDGEMENTS

This work was supported by the Federal Aviation Administration, Materials and Structures Branch, AAR-450, located at the William J. Hughes Technical Center, Atlantic City International Airport, New Jersey.

TABLE OF CONTENTS

Page

EXECUTIVE SUMMARY ix

1. INTRODUCTION 1

2. ANALYTICAL MODEL FOR SHOT-PEENING-INDUCED RESIDUAL STRESSES 4

   2.1 Fundamental Equations for the Elastic-Loading Process 4
   2.2 Elastic-Plastic Analysis of the Loading Process 7
   2.3 The Residual Stress After Unloading 11

3. VERIFICATION OF THE MODEL FOR SHOT-PEENING-INDUCED RESIDUAL STRESSES 15

4. INFLUENCE OF THE USUAL SHOT-PEENING PARAMETERS 18

5. MODELING FATIGUE CRACK GROWTH IN SHOT-PEENED STRUCTURAL COMPONENTS 26

   5.1 Modification of the NASGRO Model 29
   5.2 Plastic Strip Model 41
   5.3 Plastic Zone Model 47

6. CONCLUSIONS 52

7. REFERENCES 53

APPENDICES

A—AGILE 3D's Capabilities in Fracture Mechanics Analysis
B—Experiments (University of Washington)

LIST OF FIGURES

Figure Page

1 Elastic Contact 4

2 Elastic-Plastic Contact Indentation 9

3 The Relation of the Plastic Radius a_p vs the Shot Velocity 9

4 Schematic Diagram for Calculating Residual Stress 10

5 Flow Chart of the Model 14

6 Multilinearization of Stress-Strain Curve 15

7 Comparison of Theoretical and Experimental Results for Specimen B1, $R = 0.55$ mm, $V = 36.58$ m/s 16

8 Comparison of Theoretical and Experimental Results for Specimen B2, $R = 0.275$ mm, $V = 63.58$ m/s 17

9 Comparison of Theoretical and Experimental Results for Specimen D1, $R = 0.55$ mm, $V = 30.65$ m/s 17

10 Comparison of Theoretical and Experimental Results for Specimen D2, $R = 0.275$ mm, $V = 50.44$ m/s 17

11 The Residual Stress Distribution for Specimen A1 19

12 The Residual Stress Distribution for Specimen A2 19

13 The Residual Stress Distribution for Specimen B1 20

14 The Residual Stress Distribution for Specimen B2 20

15 The Residual Stress Distribution for Specimen C1 21

16 The Residual Stress Distribution for Specimen C2 21

17 The Residual Stress Distribution for Specimen D1 22

18 The Residual Stress Distribution for Specimen D2 22

19 The Residual Stress Distribution for 7075 Aluminum, $R = 0.6$ mm 23

20 The Residual Stress Distribution for 7075 Aluminum, $R = 0.3$ mm 23

21 General Influence of Shot-Peening Parameters on the Distribution of Residual Stresses 24

22 The Influence of the Velocity of the Sphere on the Maximal Value of the Compressive Residual Stress 24

23 The Influence of the Velocity of the Sphere on the Size of the Compressive Residual Stress Zone 25

24 The Influence of the Yield Strength of the Workpiece on the Distribution of the Residual Stress 25

25 Crack Growth Without Shot Peening 27

26 Crack Growth in Shot-Peened Structural Components 27

27 Fatigue Crack Growth 28

28 The Effect of the Residual Stress 31

29 The SENB Specimen 32

30 Crack-Tunneling Profile of a Fatigued 2024-T351 SENB Specimen, Specimen A3 34

31 Measured Crack Profiles of Three Fatigued As-Received 2024-T351 SENB Specimens 34

32 The Global FEM Model 35

33 The BEM Model in the Crack Plane 35

34 Crack Profiles for Test A2 36

35 Crack Profiles for Test A3 36

36 Crack Profiles for Test A4 37

37 The Comparison Between Numerical and Experimental Results for the Crack Profiles 37

38 Double-Edged Notch Specimen 38

39 The Residual Stress Distribution for 7075 Aluminum 38

40 The Global FEM Model 39

41 The BEM Model in the Crack Plane 40

42 The Crack Profiles for Shot-Peened and Not Shot-Peened Specimens 40

43 The Effect of Shot Peening on Crack Growth 41

44 Plastic Strip Model for a Crack (1) Initial Crack, (2) Plastic Stretch, and (3) Plastic Zone 41

45 Schematic of the Elastic-Plastic Situation Near Fatigue Crack Tip at Maximum Loads in the Fatigue Cycle 42

46 Schematic of the Elastic-Plastic Situation Near Fatigue Crack Tip at Minimum Loads in the Fatigue Cycle 43

47 Constant-Amplitude Cyclic Load With an Overload 49

48 Plastic Zone Formed at the Crack Tip Following an Overload 49

LIST OF TABLES

Table Page

1 Fatigue Crack Profile of As-Received 2024-T351 SENB Specimens, $R = 0.1$ 33

EXECUTIVE SUMMARY

To improve the fatigue life of metallic components, especially in the airframe industry, shot peening is widely used. Shot peening is a cold-working process primarily used to extend the fatigue life of metallic structural components. There is an interest from aircraft industry for the advancement of numerical algorithms and methodologies for the estimation of residual stresses due to shot peening and for the prediction of fatigue life of the shot-peened structural components.

This report describes an analytical model that was developed to simulate the shot-peening process and estimate the residual stress field in the surface layer. A numerical approach for the prediction of crack growth rates for cracks in compressive stress fields was implemented in AGILE 3D. AGILE 3D is an accurate and efficient tool for predicting nonplanar three-dimensional (3D) fatigue crack growth in airframe structural components. AGILE 3D predictions of 3D fatigue growth compared well with the University of Washington test data. The effect of shot peening on crack growth rates of various materials was investigated numerically using AGILE 3D.

Various fatigue crack growth models, including the plastic strip model and the plastic zone model, are discussed.

1. INTRODUCTION.

Shot peening is a cold-working process primarily used to extend the fatigue life of metallic structural components. Small spherical particles, typically made of hard metal, are used to impact the surface of the structural component at a velocity of 40-70 m/s. The shot-peening process consists of multiple repeated impacts of a structural component by these hard spheres. As a result of these impacts, the structural component undergoes local plastic deformation. The elastic subsurface layers should theoretically recover to their original shape during unloading, however, continuity conditions between the elastic and the plastic zones do not allow for this to occur. Consequently, a compressive residual stress field is developed in the near-surface layer of the structural component. Since fatigue cracks generally propagate from the surface of structural components, the resulting surface compressive residual stress field is highly effective in improving the early fatigue behavior of metals. The compressive residual stress field can significantly decrease the crack growth rate of short surface cracks, therefore, inherently extending the fatigue life of shot-peened structural components.

Substantial experimental studies regarding residual stress distributions, the fatigue life of shot-peened structures, and the influence of the processing parameters in relation to shot-peening effectiveness have been conducted. While computer simulations of the shot-peening process and the fatigue life prediction for shot-peened components have also begun to receive attention in scientific literature, a comprehensive review of the current status of analytical and numerical approaches to both the modeling of the shot-peening process and the fatigue life prediction of shot-peened components reveals that the general field of shot peening is insufficiently developed. Further advancements in analytical and numerical algorithms, methodologies for estimating residual stresses due to shot peening, and the prediction of fatigue life of shot-peened structural components are clearly warranted.

The shot-peening process is considerably complex: the system is dynamic and includes contact. Despite the complicated nature of the problem, there were attempts to determine the residual stress field using approximate approaches and closed form solutions [1 and 2]. Using the Hertzian contact theory and an approximate elastic-plastic analysis for the surface layer allows the estimation of the distribution of the compressive residual stress field due to shot peening. It is, however, difficult to find the appropriate boundary conditions for the solution of the quasi-static problem. One approach to overcoming this difficulty is to perform shot peening with a low coverage of the material surface, and then to estimate the force for the contact problem by measuring the size of the shot dents [1]. It was determined [1] that it is more difficult to obtain good results for aluminum alloys because they show a complex hardening evolution.

Hertz's and Davis' contact theory furnishes the only relevant analytical solution: the static contact of a rigid sphere on an elastic semi-infinite space [3 and 4]. Residual stress distributions with better precision can be obtained by using numerical methods and computer simulation of the shot-peening process. The finite element method is the most suitable modeling method because of its reliability and the possibility to implement complex material constitutive models. Some recent publications [5-8] show the potential of the finite element method for shot-peening simulation. Many authors have proposed numerical solutions for the contact between a single sphere and an elastic-plastic half space, in the static and dynamic cases (a review can be found in references 9 and 10). Meguid, et al. [8] presented a detailed analysis of two indentations on a semi-infinite medium, under dynamic conditions. Very few studies present the analysis of shot peening modeled by multiple indentations.

The shot-peening simulation can be performed during one finite element dynamic elastic-plastic analysis. However, such an approach appears to be computationally inefficient. Typically, the shot-peening simulation is divided into two steps. The first step is a dynamic analysis of the shot workpiece contact, which is aimed at the determination of boundary conditions for the second elastic-plastic step. The second step is a quasi-static elastic-plastic analysis, which produces the distribution of residual stresses. In reference 5 the dynamic contact problem for one shot is solved as an axisymmetric one. Displacements at the contact surface are used as boundary conditions for the three-dimensional (3D) elastic-plastic multishot problem.

A similar approach to the shot peening modeling is included in reference 6. Numerical analyses have been performed using the finite element package ABAQUS. The contact of a single shot with a semi-infinite medium is the first step in modeling the shot-peening process. The problem is axisymmetric, and a two-dimensional finite element model is used. The maximum penetration obtained with the dynamic analysis is used as a boundary condition for the quasi-static, elastic-plastic computation. Up to four impacts have been modeled in a 3D elastic-plastic analysis. It was shown that the difference between a three- and four-impact solution is small enough. Comparison of numerically determined residual stresses with experimental results for aluminum and steel showed some differences (a finite element solution predicts higher absolute values of residual stresses). The difference can be explained by the following factors: neglecting friction in numerical modeling and using the normal direction for the impact (in industrial peening, the vector of the shot is rarely normal to the surface).

The effect of shot velocity, size, and shape on the residual stresses of a target exhibiting bilinear material behavior is examined in references 7 and 8. The 3D dynamic elastic-plastic analysis was performed using the finite element code ANSYS. Dynamic single and twin elastic-plastic spherical indentations were examined using rigid spherical shots and metallic targets. The results revealed that near-surface residual stresses were significantly influenced by the shot velocity, shot shape, and separation distance between the coindenting shots and to a much lesser extent by the strain-hardening rate of the target. It was also shown that the large variability in residual stress distribution results from either incomplete coverage or variability of the shape of the shot.

An enormous amount of research has been conducted on the subject of shot peening; however, the majority had been experimental in nature. Perhaps this topic of research had been overlooked due to difficulties associated with predicting the complex manner in which the target material responds to the multi-impact of shots. Although the early experiments promoted the understanding of the theoretical and physical issues of the peening process, shot peening remains a controversial field [11].

Based on an elastic perfectly plastic body, Al-Hassani [12, 13, and 9] developed an analysis model to predict residual stresses, which depend on the experimental results (there exist empirical relations to fit experimental results) to obtain certain critical relations. Guechichi, et al. [14] proposed a very complex model for elastic-plastic body. Li, et al. [2] developed a simplified analytical model for an elastic-plastic body by regarding the shot-peening process as a quasi-static case, which cannot take the velocity of the shot into account and, in addition, depends on empirical parameters to develop a theoretical model. A new theoretical model has been developed based on the initial models of references 13 and 2. Principal developments were made to take the primary shot-peening factors into consideration (e.g., characteristics of the material, diameter, and velocity of the shot).

Several investigators have studied the effects of shot peening on crack growth behavior, yet the results are conflicting. Moutoh, et al. [15] and Kopsov [16] found that crack initiation lives were longer in the unpeened specimens, while the total fatigue lives were longer for the peened specimens. On the contrary, the crack initiation lives and total fatigue lives were both favored under peened conditions in the study by De los Rios, et al. [17]. In fact, various governing factors such as peening parameters and the definition of crack initiation lives were supposed to play a role in the crack growth behavior [18 and 19]. However, the shot-peening treatment of the material surface is proven to appreciably enhance the fatigue life of structural components. The presence of the compressive residual stresses in the near-surface layers of service components were found to considerably retard the fatigue crack growth rates. Experimental data of fatigue life extension for structural components made of steel and aluminum can be found in reference 20. Song, et al. [21] investigated the fatigue crack propagation behavior of compact tension specimens of AISI 304 stainless steel after shot peening while also considering and the crack closure effect.

Presently, it is difficult to expect that direct numerical modeling of elastic-plastic fatigue growth of small cracks can produce sufficiently accurate practical results. The practical way of modeling fatigue crack growth in shot-peened structural components could consist of (1) using efficient numerical method for computing fracture mechanics parameters for the crack and (2) employing approximate approaches based on a plastic strip model for predicting crack growth rates.

The plasticity and crack-closure effects during fatigue growth of a crack can be analyzed numerically, using finite element methods (FEM). Such an approach has been developed in the papers of Nakagaki and Atluri [22], and Newman, et al. [23]. Application of the plastic strip models for modeling of small fatigue crack growth is considered in references 24 and 25. According to the plastic strip model, near-tip plastic yielding was assumed to be localized in thin strips near the crack tips. These plastic strips were modeled as additional discontinuities in order to satisfy plasticity conditions. The rest of the body was considered to be elastic. In reference 24, the plastic strip model is combined with a method of singular integral equations for predicting growth of small fatigue cracks. In reference 25, the plastic strip model was extended to incorporate the effects of shot peening. The crack was divided into three zones: the crack, the plastic zone, and the barrier zone (grain boundary). The extended plastic strip model can take into account both the effects of residual stresses and those imposed by the materials microstructure both of which can be affected by the shot-peening process.

The following objectives were the focus of this research:

1. Development of a methodology for modeling the shot-peening process and estimating the residual stress field in the surface layer.

2. Development of a numerical approach for the prediction of crack growth rates for short cracks in compressive stress fields.

3. Numerical investigation of the effect of shot peening on crack growth rates of various materials; development of a database containing results.

4. Validation of developed software tools for prediction of fatigue life of shot-peened parts used in principal structural elements.

2. ANALYTICAL MODEL FOR SHOT-PEENING-INDUCED RESIDUAL STRESSES.

2.1 FUNDAMENTAL EQUATIONS FOR THE ELASTIC-LOADING PROCESS.

It is assumed that the shot-peened part (target material) is a semifinite body. A homogeneous residual stress field and associated plastic strain exist at any specified depth due to the assumption that a semifinite body has been uniformly loaded. To describe the maximum elastic loading, the impact of an elastic sphere on the surface of an elastic semifinite body is analyzed. This can be considered as a particular application of the Hertzian contact theory between two elastic spheres. A schematic is shown in figure 1.

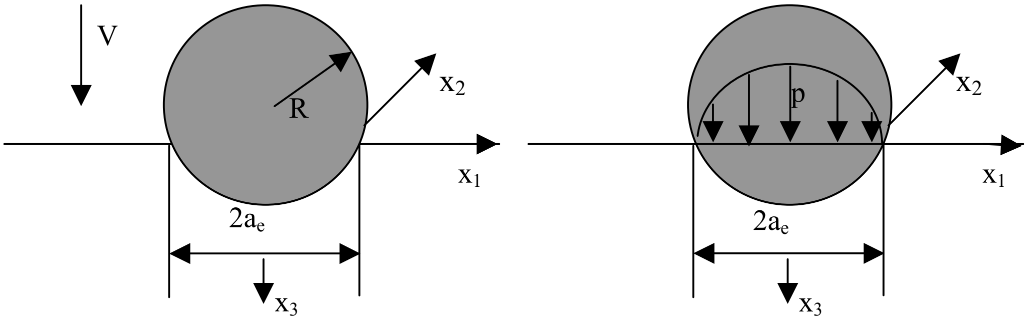

FIGURE 1. ELASTIC CONTACT

According to the Hertzian contact theory, when the elastic compression is at its maximum, the radius of the elastic contact circle between the shot and the semifinite body, is expressed as

$$a_e = R\left[\frac{5}{2}\pi k\rho\frac{V^2}{E_0}\right]^{\frac{1}{5}} \tag{1}$$

and the maximum normal elastic pressure is given by

$$p = \frac{1}{\pi}\left[\frac{5}{2}\pi k \rho V^2 E_0^4\right]^{\frac{1}{5}} \tag{2}$$

These two equations were initially proposed in Davies' work [3] on dynamic elastic contact between a half space and a ball of radius R, with

$$\frac{1}{E_0} = \frac{1-\nu^2}{E} + \frac{1-\nu_s^2}{E_s} \tag{3}$$

where V is the initial velocity of the shot, p is the maximum normal pressure, R is the radius of the shot, and a_e is, at maximum, the radius of the elastic contact circle, ρ is the density of the shot, E and ν and E_s and ν_s are Young's modulus and Poisson's ratio of the target and shot, respectively. k is an efficiency coefficient that stands for the thermal and elastic dissipation during the impact. The value of k is fixed at 0.8 according to Johnson [4]. A 100% k value will describe purely elastic rebound energy.

The classical Hertz results are used to model the elastic stress field created by the impact. The Hertzian elastic stress tensor can be written as follows:

$$\mathbf{T}^e = \begin{bmatrix} \sigma_{11}^e & 0 & 0 \\ 0 & \sigma_{22}^e & 0 \\ 0 & 0 & \sigma_{33}^e \end{bmatrix}$$

where the subscripts 1, 2, and 3 represents the axis x_1, x_2, and x_3, respectively. The elastic stress field is then obtained from the Hertzian theory. The stresses in the target material reach their maximum under the shot and can be written as

$$\begin{aligned} \sigma_{11}^e &= p(1+\nu)\left[\frac{x_3}{a_e}\tan^{-1}\left(\frac{x_3}{a_e}\right) - 1\right] + p\frac{a_e^2}{2\left(a_e^2 + x_3^2\right)} \\ \sigma_{22}^e &= p(1+\nu)\left[\frac{x_3}{a_e}\tan^{-1}\left(\frac{x_3}{a_e}\right) - 1\right] + p\frac{a_e^2}{2\left(a_e^2 + x_3^2\right)} \end{aligned} \tag{4}$$

$$\sigma_{33}^e = -p\left[1 + \left(\frac{x_3}{a_e}\right)^2\right]^{-1} \tag{5}$$

According to Hook's law, the strains are expressed as

$$\begin{aligned} \varepsilon_{11}^{e} &= \frac{1}{E}\left[\sigma_{11}^{e} - v\left(\sigma_{22}^{e} + \sigma_{33}^{e}\right)\right] \\ \varepsilon_{22}^{e} &= \frac{1}{E}\left[\sigma_{11}^{e} - v\left(\sigma_{22}^{e} + \sigma_{33}^{e}\right)\right] \end{aligned} \tag{6}$$

$$\varepsilon_{33}^{e} = \frac{1}{E}\left[\sigma_{33}^{e} - 2v\sigma_{11}^{e}\right] \tag{7}$$

Thus, one can obtain the Von Mises equivalent stress in the target material as

$$\sigma_{i}^{e} = \left[\left(\sigma_{11}^{e} - \sigma_{22}^{e}\right)^{2} + \left(\sigma_{22}^{e} - \sigma_{33}^{e}\right)^{2} + \left(\sigma_{33}^{e} - \sigma_{11}^{e}\right)^{2}\right]^{\frac{1}{2}} \Big/ \sqrt{2} \tag{8}$$

Then, the equivalent strain can be obtained through Hook's law as

$$\varepsilon_{i}^{e} = \frac{\sigma_{i}^{e}}{E} \tag{9}$$

The mean stress and strain can be written as

$$\begin{aligned} \sigma_{m}^{e} &= \frac{1}{3}\left(\sigma_{11}^{e} + \sigma_{22}^{e} + \sigma_{33}^{e}\right) \\ \varepsilon_{m}^{e} &= \frac{1}{3}\left(\varepsilon_{11}^{e} + \varepsilon_{22}^{e} + \varepsilon_{33}^{e}\right) \end{aligned} \tag{10}$$

Now, the stress deviators in the target material can be derived as

$$\begin{aligned} s_{11}^{e} &= \sigma_{11}^{e} - \sigma_{m}^{e} = \frac{1}{3}\sigma_{i}^{e} \\ s_{22}^{e} &= \sigma_{22}^{e} - \sigma_{m}^{e} = \frac{1}{3}\sigma_{i}^{e} \end{aligned} \tag{11}$$

$$s_{33}^{e} = \sigma_{33}^{e} - \sigma_{m}^{e} = -\frac{2}{3}\sigma_{i}^{e} = -2s_{11}^{e} \tag{12}$$

Similar to the stress deviators, the strain deviators are derived as

$$e_{11}^{e} = \varepsilon_{11}^{e} - \varepsilon_{m}^{e} = \frac{1}{3}(1+v)\varepsilon_{i}^{e}$$
$$e_{22}^{e} = \varepsilon_{22}^{e} - \varepsilon_{m}^{e} = \frac{1}{3}(1+v)\varepsilon_{i}^{e} \tag{13}$$

$$e_{33}^{e} = \varepsilon_{33}^{e} - \varepsilon_{m}^{e} = -\frac{2}{3}(1+v)\varepsilon_{i}^{e} = -2e_{11}^{e} \tag{14}$$

Therefore, the stress and strain tensors in the elastic field are now derived. The elastic-plastic analysis of the loading process will be discussed in the subsequent section.

2.2 ELASTIC-PLASTIC ANALYSIS OF THE LOADING PROCESS.

The elastic-plastic regime presents a difficult theoretical problem that is still a subject of serious research effort. In the elastic-plastic deformation stage, the equivalent stress in the target material is greater than the yield stress, i.e., $\sigma_i > \sigma_s$; the stress-strain analysis becomes too complicated and inconvenient to apply in practice. It is very difficulty to directly use the complex elastic-plastic constitutive relation in engineering. It is, however, worth resorting to a simple analytical treatment. As in many elastic-plastic analyses, the elastic-plastic constitutive relationship associated with the target material can be simplified to a multilinear one. A simplified relation [2] will be implemented here. By adopting a modifying coefficient, $\overline{\alpha}$, the elastic-plastic strain ε_i^p at any depth x_3 is calculated from the elastic strain ε_i^e, at the corresponding depth x_3:

$$\varepsilon_i^p = \begin{cases} \varepsilon_i^e & \text{for } \varepsilon_i^e \le \varepsilon_s \\ \varepsilon_s + \overline{\alpha}\left(\varepsilon_i^e - \varepsilon_s\right) & \text{for } \varepsilon_i^e > \varepsilon_s \end{cases} \tag{15}$$

where ε_i^p and ε_i^e are functions of x_3 only, ε_s is the strain corresponding to the yield stress σ_s, and $\overline{\alpha}$ is the ratio of plastic to elastic deformation and is defined as

$$\overline{\alpha} = \frac{a_p}{a_e} \tag{16}$$

where a_e is given in equation 1, and a_p is the radius of a dent produced by the same shot on an elastic-plastic target under the same velocity. It is assumed that the ratio of ε_i^p to ε_i^e on the z axis inside the target is equal to the ratio α of the deformation at the surface.

The derivation of the plastic radius a_p begins with the equation of motion during contact.

$$\frac{4\pi}{3}\rho R^3\frac{dV}{dt}=-\pi a^2\overline{p} \tag{17}$$

The elastic-plastic contact indentation is shown in figure 2. As in reference 13, the stress field surrounding the indentation is assumed to be the same as for a pressurized spherical cavity in an elastic-plastic material. The cavity expands to accommodate the material displaced by the indenter. The model gives an approximate value for the average pressure $\overline{p}$ resisting the motion [13], as

$$\frac{\overline{p}}{\sigma_s}=0.6+\frac{2}{3}\ln\frac{Ea}{\sigma_s R} \tag{18}$$

It then follows that

$$\frac{\overline{z}}{R}=\left(\frac{2}{3}\right)^{\frac{1}{2}}\left(\frac{\rho V^2}{\overline{p}}\right)^{\frac{1}{2}}Q(\overline{z}) \tag{19}$$

Where

$$1/Q=\left[\left(0.2+\frac{2}{9}ln\frac{E}{\sigma_s}\right)+\frac{1}{9}\left(ln\frac{2\overline{z}}{R}-\frac{4\overline{z}}{R}\right)\right]^{\frac{1}{2}}$$

and $\overline{z}$ is the final indentation [13]. This equation governs the initial stages of deformation but as soon as the pressure $\overline{p}$ reaches $3\sigma_s$, a rigid plastic analysis will hold. This may be found theoretically and has also received considerable experimental confirmation. By assuming pressure $\overline{p}$ to remain constant during the indentation process, equation 19 will become

$$\frac{\overline{z}}{R}=\left(\frac{2}{3}\right)^{\frac{1}{2}}\left(\frac{\rho V^2}{\overline{p}}\right)^{\frac{1}{2}}$$

By means of

$$a^2=2\overline{z}R-\overline{z}^2 \tag{20}$$

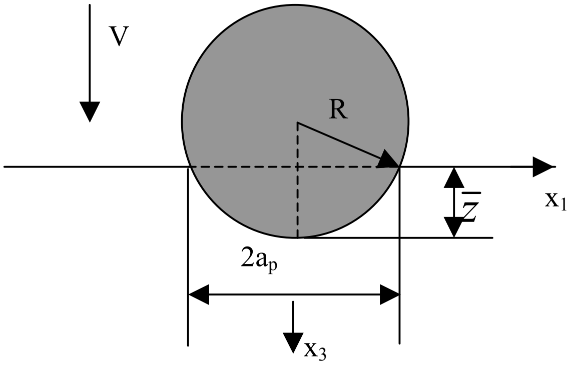

FIGURE 2. ELASTIC-PLASTIC CONTACT INDENTATION

A nonlinear equation of *a* is now formed, and the plastic radius a_p can be obtained by solving this nonlinear equation. These equations are derived for elastic-perfect plastic materials but are still used to approximate the plastic radius a_p for strain-hardened materials.

The relation between the shot velocity and the plastic radius a_p can be obtained from these equations, as shown in figure 3. It is reasonable that the plastic radius a_p increases as the shot velocity increases.

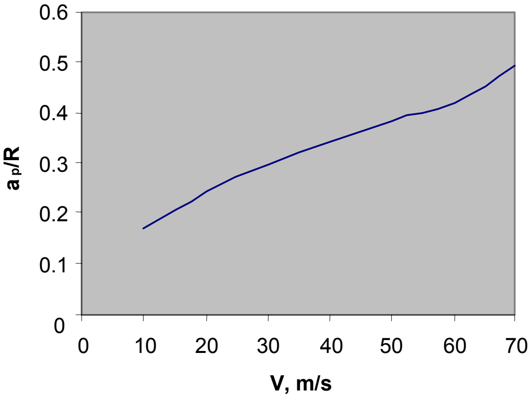

FIGURE 3. THE RELATION OF THE PLASTIC RADIUS a_p VS THE SHOT VELOCITY

According to the elastic-plastic, stress-strain curve (multilinear), the elastic-plastic stress σ_i^p is calculated as

$$\sigma_i^p = \begin{cases} \sigma_i^e & \text{for } \varepsilon_i^p < \varepsilon_s \\ \sigma_s + E_1\left(\varepsilon_i^p - \varepsilon_s\right) & \text{for } \varepsilon_s \le \varepsilon_i^p < \varepsilon_b \\ \sigma_b & \text{for } \varepsilon_i^p \ge \varepsilon_b \end{cases} \tag{21}$$

The definitions of the parameters are shown in figure 4, and σ_b is the ultimate tension strength.

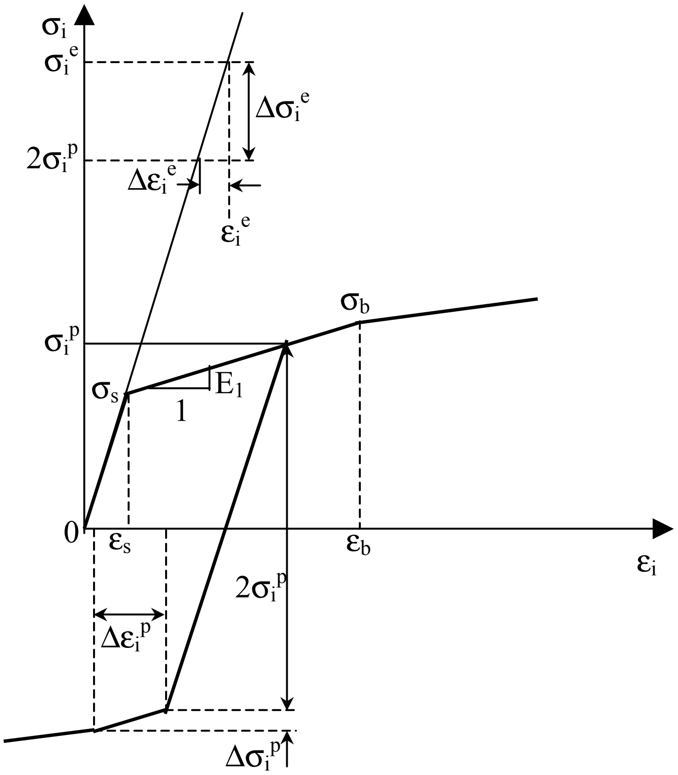

FIGURE 4. SCHEMATIC DIAGRAM FOR CALCULATING RESIDUAL STRESS

To obtain the stress deviators, one should derive the strain deviators first. Due to the fact that the relationship between the strain deviators and ε_i^e, as in equations 13 and 14 for the elastic stage results from the axisymmetry of loading and geometric conditions, the corresponding relationship in the elastic-plastic stage will be kept the same. Hence, the elastic-plastic strain deviators can be expressed as

$$
\begin{aligned}
e_{11}^p &= \frac{1}{3}(1+v)\varepsilon_i^p \\
e_{22}^p &= \frac{1}{3}(1+v)\varepsilon_i^p
\end{aligned}
\tag{22}
$$

$$e_{33}^p = -\frac{2}{3}(1+v)\varepsilon_i^p = -2e_{11}^p \tag{23}$$

By appealing to the elastic-plastic theory, the elastic-plastic stress deviators can be derived from the following relationship

$$s_{ij}^p = \frac{1}{1+v}\frac{\sigma_i^p}{\varepsilon_i^p}e_{ij}^p \tag{24}$$

Thus, the elastic-plastic stress deviators can be obtained as

$$s_{11}^{p} = \frac{1}{1+v}\frac{\sigma_i^p}{\varepsilon_i^p}e_{11}^{p} = \frac{1}{3}\sigma_i^p$$
$$s_{22}^{p} = \frac{1}{1+v}\frac{\sigma_i^p}{\varepsilon_i^p}e_{22}^{p} = \frac{1}{3}\sigma_i^p \tag{25}$$

$$s_{33}^{p} = -\frac{2}{3}\sigma_i^p = -2s_{11}^{p} \tag{26}$$

Now, the stress and strain tensors in the elastic-plastic field are obtained. An expression will be derived for the residual stress field after unloading, in the next section.

2.3 THE RESIDUAL STRESS AFTER UNLOADING.

Similar to reference 2, three assumptions are involved: (1) the deformation is small, (2) unloading is an elastic process before reversed yielding starts, and (3) hydrostatic stresses do not introduce plastic deformation. By means of these assumptions, the basic formula for calculating the residual stress can be written as

$$\sigma_{ij}^{r} = s_{ij}^{p} - s_{ij}^{e} \tag{27}$$

The shot-peened material (target material) is assumed to be isotropic. Therefore, the residual stresses can be derived from the following relation

$$\sigma_{ij}^{r} = \begin{cases} 0 & \text{for } \sigma_i^e \le \sigma_s \\ s_{ij}^{p} - s_{ij}^{e} & \text{for } \sigma_{\mathrm{s}} \le \sigma_i^e < 2\sigma_i^p \end{cases} \tag{28}$$

which illustrates that there is no residual stress in the elastic-loading stage. Thus, the residual stresses can be expressed as

$$\sigma_{11}^{r} = \frac{1}{3}\left(\sigma_i^p - \sigma_i^e\right)$$
$$\sigma_{22}^{r} = \frac{1}{3}\left(\sigma_i^p - \sigma_i^e\right) \quad \text{for } \sigma_s \le \sigma_i^e \le 2\sigma_i^p \tag{29}$$
$$\sigma_{33}^{r} = -2\sigma_{11}^{r}$$

The target material will experience reversed yielding and hardening if $\sigma_i^e \ge 2\sigma_i^p$. Figure 4 shows schematically how to calculate σ^r. A stress of $2\sigma_i^p$ is elastically unloaded first, then reversed yielding take place, but there are still some stresses that have not been unloaded, as shown in figure 4, which can be expressed as

$$\Delta\sigma_i^e = \sigma_i^e - 2\sigma_i^p \tag{30}$$

From Hook's law and the assumption that the ratio of ε_i^p to ε_i^e on the x_3 axis inside the target is equal to the ratio α of the deformation at the surface, the elastic and elastic-plastic strains corresponding to $\Delta\sigma_i^e$ are obtained, respectively, as

$$\Delta\varepsilon_i^e = \frac{\Delta\sigma_i^e}{E} \tag{31}$$

$$\Delta\varepsilon_i^p = \alpha\Delta\varepsilon_i^e \tag{32}$$

Then, as in figure 4, the corresponding stress $\Delta\sigma_i^p$ can be obtained by using the multilinear stress-strain curve. Thus, the residual stress can be obtained as

$$\begin{aligned}
\sigma_{11}^r &= \frac{1}{3}\left(\sigma_i^p - 2\sigma_i^p - \Delta\sigma_i^p\right) \\
\sigma_{22}^r &= \frac{1}{3}\left(\sigma_i^p - 2\sigma_i^p - \Delta\sigma_i^p\right) \\
\sigma_{33}^r &= -2\sigma_{11}^r
\end{aligned} \tag{33}$$

σ^r is only the residual stress after loading and unloading a single ball. After shot peening once on the whole surface, i.e., 100% coverage, it is assumed that the plastic deformation is steady and continuous. As there is no particular direction on the surface of the semi-infinite body, all the tensors depend only on the depth x_3. The residual stress tensor in the stabilized state is independent of the coordinates (x_1, x_2) and remains constant on any plane parallel to the surface, with $\sigma_{11}^R = \sigma_{22}^R$. The superscript R indicates the residual stress after 100% coverage, i.e., the final residual stress. The boundary conditions on the surface enable one to write

$$\sigma_{13}^R(0) = \sigma_{23}^R(0) = \sigma_{33}^R(0) = 0$$

The equilibrium equations are reduced to

$$\frac{\partial\sigma_{13}^R}{\partial x_3} = 0$$

$$\frac{\partial\sigma_{23}^R}{\partial x_3} = 0$$

$$\frac{\partial \sigma_{33}^R}{\partial x_3} = 0$$

So at any depth x_3 one has

$$\sigma_{12}^R(x_3) = \sigma_{13}^R(x_3) = \sigma_{23}^R(x_3) = \sigma_{33}^R(x_3) = 0$$

The equilibrium equations and the boundary conditions for the residual stresses lead to the following residual tensor expression as

$$\mathbf{S}^R = \begin{bmatrix} \sigma_{11}^R(x_3) & 0 & 0 \\ 0 & \sigma_{11}^R(x_3) & 0 \\ 0 & 0 & 0 \end{bmatrix}$$

Hence, the residual stress and strain fields can be obtained as

$$\begin{aligned} \sigma_{11}^R &= \sigma_{22}^R = f(x_3) \\ \sigma_{33}^R &= 0 \\ \varepsilon_{11}^R &= \varepsilon_{22}^R = 0 \\ \varepsilon_{33}^R &= g(x_3) \end{aligned} \tag{34}$$

It is noted that the stresses (equation 33) fail to satisfy the equilibrium conditions. To obtain the correct residual stress field, equation 33 must be partially relaxed. By means of Hooke's law, the relaxation values of σ_{11}^r and σ_{22}^r, i.e., $\sigma_{11}^{'}$ and $\sigma_{22}^{'}$, can be obtained as

$$\begin{aligned} \sigma_{11}^{'} &= \frac{v}{1-v}\sigma_{33}^r \\ \sigma_{22}^{'} &= \frac{v}{1-v}\sigma_{33}^r \end{aligned} \tag{35}$$

Thus, the final residual stressed σ_{11}^R and σ_{22}^R can be obtained as

$$\begin{aligned} \sigma_{11}^R &= \sigma_{11}^r - \frac{v}{1-v}\sigma_{33}^r = \frac{1+v}{1-v}\sigma_{11}^r \\ \sigma_{22}^R &= \sigma_{22}^r - \frac{v}{1-v}\sigma_{33}^r = \frac{1+v}{1-v}\sigma_{11}^r \end{aligned} \tag{36}$$

The above procedure is similar to that in reference 2. However, it is noted that in reference 2, they assume the shot-peening procedure is a static phenomenon, so they did not consider the effect of the velocity. Their model is an empirical relation between the plastic radius a_p of the dent and the equivalent static load F of shot peening, which is extracted by fitting experimental results. The quantity a_p is measured directly from experimental data and then applied using the empirical relation to evaluate the equivalent static load of shot peening, F. No empirical relations are used in the analyses discussed in this newly developed model because the quantity a_p is determined by the shot velocity. Therefore, this model is more reasonable, convenient, and simple than that of reference 2.

It is easy to implement the aforementioned theory to calculate the residual stresses due to shot peening. The flow chart of the newly developed model is shown in figure 5.

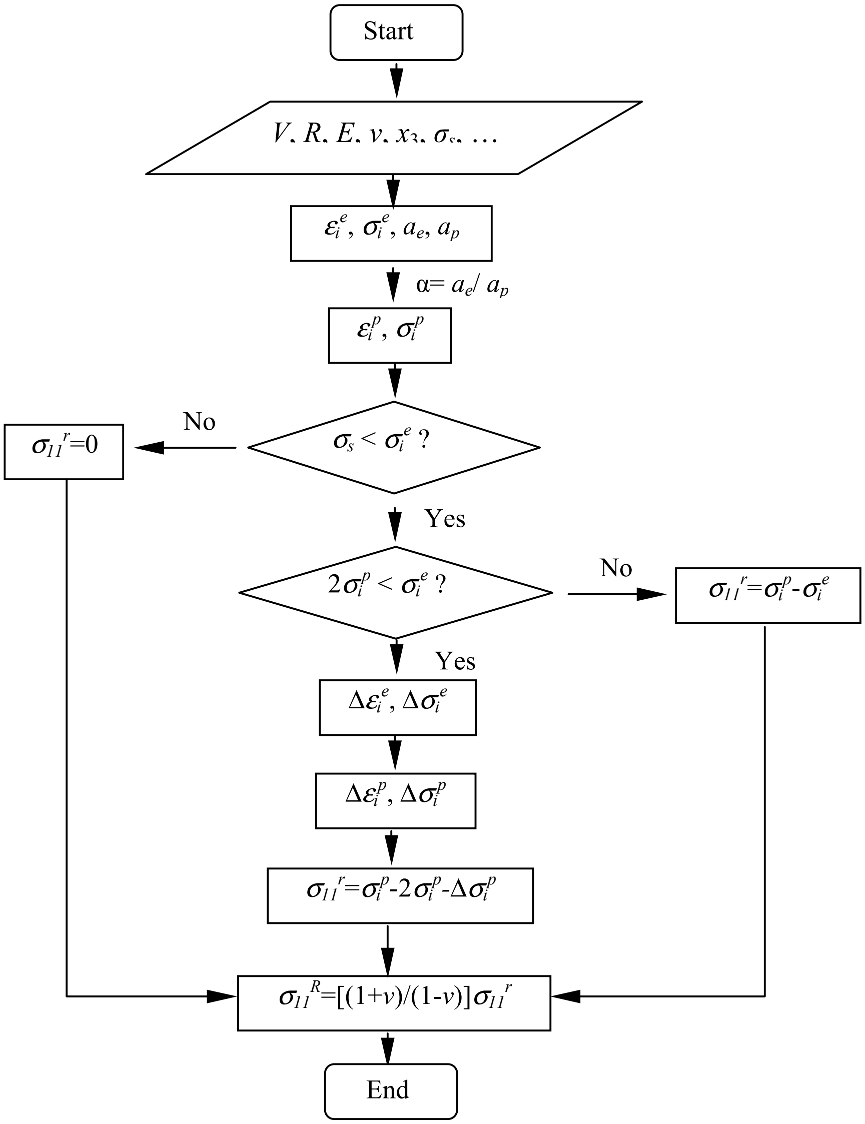

Start
$V, R, E, \nu, x_3, \sigma_s, \ldots$
$\varepsilon_i^e, \sigma_i^e, a_e, a_p$
$\alpha = a_e / a_p$
$\varepsilon_i^p, \sigma_i^p$
No
$\sigma_{11}{}^r = 0$
$\sigma_s < \sigma_i^e$?
Yes
$2\sigma_i^p < \sigma_i^e$?
No
$\sigma_{11}{}^r = \sigma_i^p - \sigma_i^e$
Yes
$\Delta\varepsilon_i^e, \Delta\sigma_i^e$
$\Delta\varepsilon_i^p, \Delta\sigma_i^p$
$\sigma_{11}{}^r = \sigma_i^p - 2\sigma_i^p - \Delta\sigma_i^p$
$\sigma_{11}{}^R = [(1+\nu)/(1-\nu)]\sigma_{11}{}^r$
End

FIGURE 5. FLOW CHART OF THE MODEL

3. VERIFICATION OF THE MODEL FOR SHOT-PEENING-INDUCED RESIDUAL STRESSES.

To verify this model, the experimental results in reference 2 for 40Cr steel were used. The chemical composition of the 40Cr steel is 0.41C-0.72Mn-0.19Si-0.030P-0.009S-1.0Cr-0.08Ni (weight percent). The B1, B2, D1, and D2 specimens were used to verify this analysis model. All specimens are 40Cr steel but have been subjected to different chemical treatments. Their tension stress-strain curves are multilinearized and are shown schematically in figure 6. The material properties are given as follows:

- Specimen B1:

  $E = 2 \times 10^5\ MPa$, $v = 0.3$, $\sigma_s = 1270\ MPa$, $\sigma_b = 1540\ MPa$, $\varepsilon_b = 4.5 \times 10^{-2}$, $D = 1.10\ mm$

- Specimen B2:

  $E = 2 \times 10^5\ MPa$, $v = 0.3$, $\sigma_s = 1270\ MPa$, $\sigma_b = 1540\ MPa$, $\varepsilon_b = 4.5 \times 10^{-2}$, $D = 0.55\ mm$

- Specimen D1:

  $E = 2 \times 10^5\ MPa$, $v = 0.3$, $\sigma_s = 700\ MPa$, $\sigma_b = 885\ MPa$, $\varepsilon_b = 0.14$, $D = 1.10\ mm$

- Specimen D2:

  $E = 2 \times 10^5\ MPa$, $v = 0.3$, $\sigma_s = 700\ MPa$, $\sigma_b = 885\ MPa$, $\varepsilon_b = 0.14$, $D = 0.55\ mm$

where D is the thickness of the specimen.

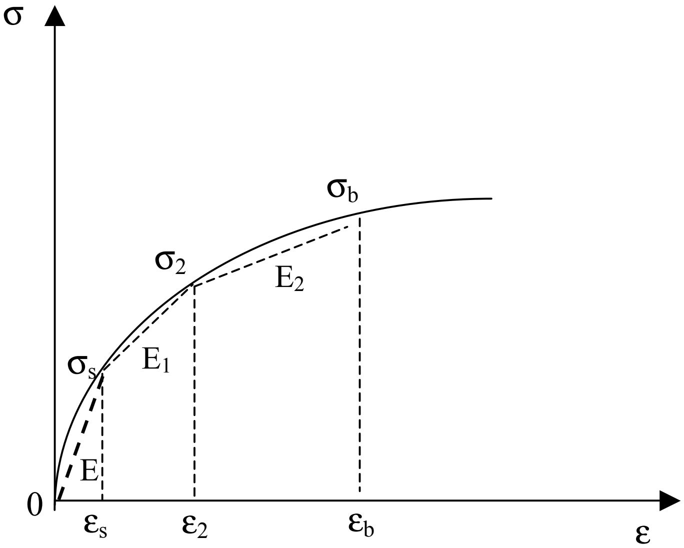

FIGURE 6. MULTILINEARIZATION OF STRESS-STRAIN CURVE

The density of the 40Cr steel is ρ = 7800 kg/m^3. The experimental results [2] did not include the velocity of the shot. However, the equivalent static load of shot peening, F, was provided. The velocity of the shot was back calculated by equaling the maximum pressure at the contact center for the static case and for the dynamic case.

For dynamic cases

$$p = \frac{1}{\pi}\left[\frac{5}{2}\pi k \rho V^2 E_0^4\right]^{\frac{1}{5}}$$

For static cases

$$p = \frac{1}{\pi}\left[\frac{3}{2} F R^{-2} E_0^2\right]^{\frac{1}{3}}$$

Then, by equaling these two equations, for a given F, (in their experiment, F = 340 N, 165 N, 275 N and 125 N for specimen B1, B2, D1, and D2, respectively) one can calculate the corresponding velocity V. Thus, the following velocity is obtained:

- V = 36.58 m/s for specimen B1
- V = 63.58 m/s for specimen B2
- V = 30.65 m/s for specimen D1
- V = 50.44 m/s for specimen D2

The comparison of the theoretical model and the experimental results are shown in figures 7 through 10, for specimens B1, B2, D1, and D2, respectively. Good agreements between this theoretical model and experimental results were found.

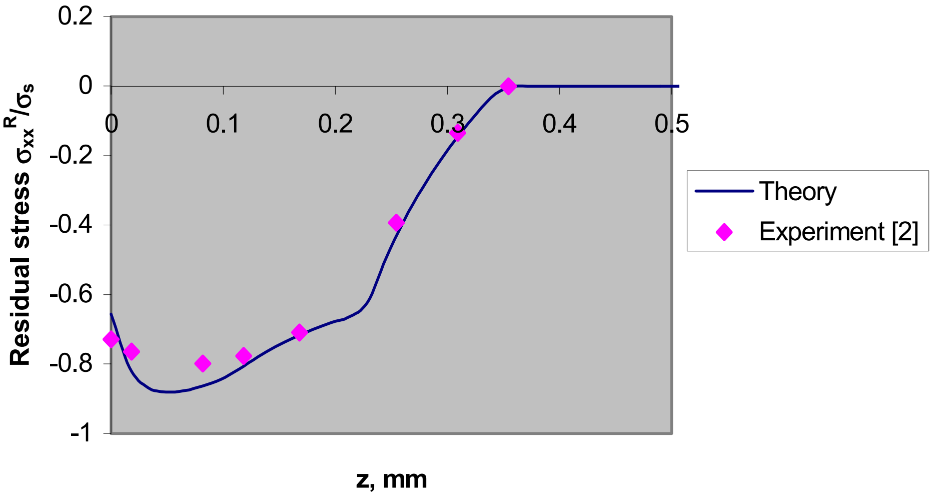

FIGURE 7. COMPARISON OF THEORETICAL AND EXPERIMENTAL RESULTS FOR SPECIMEN B1, R = 0.55 mm, V = 36.58 m/s

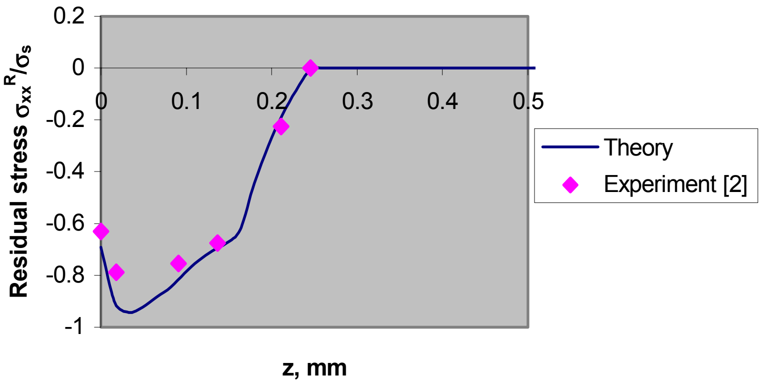

FIGURE 8. COMPARISON OF THEORETICAL AND EXPERIMENTAL RESULTS FOR SPECIMEN B2, *R* = 0.275 mm, *V* = 63.58 m/s

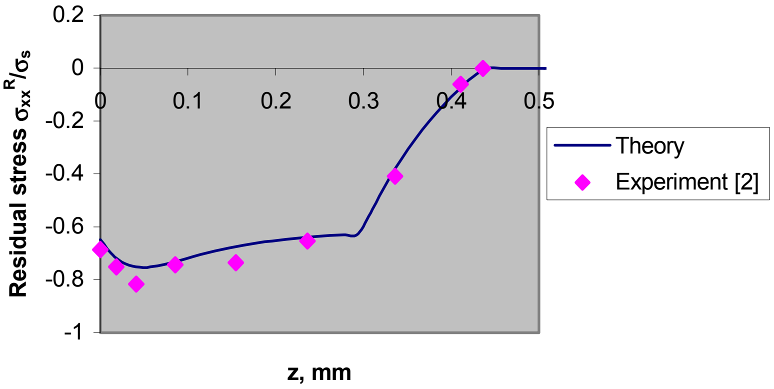

FIGURE 9. COMPARISON OF THEORETICAL AND EXPERIMENTAL RESULTS FOR SPECIMEN D1, *R* = 0.55 mm, *V* = 30.65 m/s

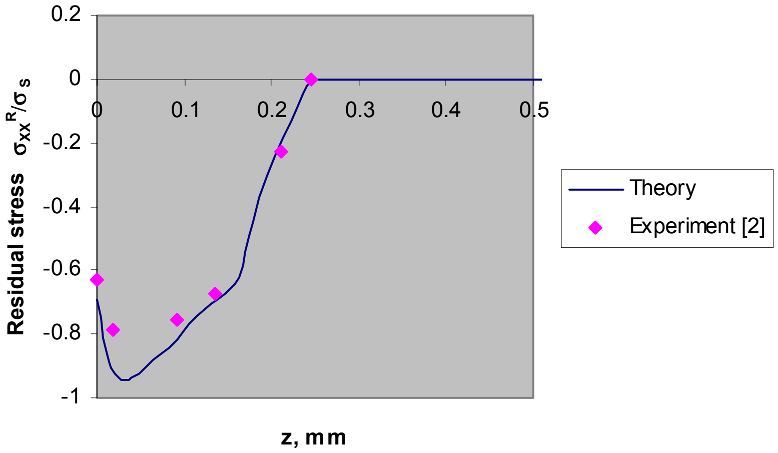

FIGURE 10. COMPARISON OF THEORETICAL AND EXPERIMENTAL RESULTS FOR SPECIMEN D2, *R* = 0.275 mm, *V* = 50.44 m/s

An effort was made to verify this model with other sets of experimental results, however, results that listed a complete set of material parameters (which are necessary for this model) were practically impossible to locate. The initial comparison demonstrates that the trends of the analysis model were reasonable and agree very well with the experimental results from reference 2.

This analysis model has advanced and generalized the solution procedure for determining the residual stresses induced by shot peening and has also provided good agreement with the experimental results obtained from reference 2 that is equivalent to that obtained with their semiempirical model.

Within reasonable accuracy, the experimentally observed effects were found in the present analytical model and very few numerical computations were necessary. A complete numerical computation, such as FEM, would have been extremely intensive, computationally inefficient, and entirely unrealistic. Therefore, the present analysis model appears to be a very suitable tool for the current study.

4. INFLUENCE OF THE USUAL SHOT-PEENING PARAMETERS.

The newly developed analysis model is used to simulate the residual stress distribution in 40Cr steels with different chemical treatments. The material properties are given as follows:

- Specimen A1:

  $E = 2 \times 10^5$ *MPa*, $v = 0.3$, $\sigma_s = 1420$ *MPa*, $\sigma_b = 1950$ *MPa*, $\varepsilon_b = 3.5 \times 10^{-2}$, $D = 1.10$ *mm*

- Specimen A2:

  $E = 2 \times 10^5$ *MPa*, $v = 0.3$, $\sigma_s = 1420$ *MPa*, $\sigma_b = 1950$ *MPa*, $\varepsilon_b = 3.5 \times 10^{-2}$, $D = 0.55$ *mm*

- Specimen B1:

  $E = 2 \times 10^5$ *MPa*, $v = 0.3$, $\sigma_s = 1270$ *MPa*, $\sigma_b = 1540$ *MPa*, $\varepsilon_b = 4.5 \times 10^{-2}$, $D = 1.10$ *mm*

- Specimen B2:

  $E = 2 \times 10^5$ *MPa*, $v = 0.3$, $\sigma_s = 1270$ *MPa*, $\sigma_b = 1540$ *MPa*, $\varepsilon_b = 4.5 \times 10^{-2}$, $D = 0.55$ *mm*

- Specimen C1:

  $E = 2 \times 10^5$ *MPa*, $v = 0.3$, $\sigma_s = 980$ *MPa*, $\sigma_b = 1210$ *MPa*, $\varepsilon_b = 6.6 \times 10^{-2}$, $D = 1.10$ *mm*

- Specimen C2:

  $E = 2 \times 10^5$ *MPa*, $v = 0.3$, $\sigma_s = 980$ *MPa*, $\sigma_b = 1210$ *MPa*, $\varepsilon_b = 6.6 \times 10^{-2}$, $D = 0.55$ *mm*

- Specimen D1:

  $E = 2 \times 10^5\ MPa,\ v = 0.3,\ \sigma_s = 700\ MPa,\ \sigma_b = 885\ MPa,\ \varepsilon_b = 0.14,\ D = 1.10\ mm$

- Specimen D2:

  $E = 2 \times 10^5\ MPa,\ v = 0.3,\ \sigma_s = 700\ MPa,\ \sigma_b = 885\ MPa,\ \varepsilon_b = 0.14,\ D = 0.55\ mm$

where D is defined as the thickness of the specimen.

The density of the 40Cr steel is $\rho = 7800$ kg/m^3. The distributions of the residual stresses under different shot velocities for different specimens are shown in figures 11 through 18 for specimens A1-D2, respectively. In all these simulations, three shot velocities were considered: $V = 10$ m/s, 30 m/s, and 60 m/s.

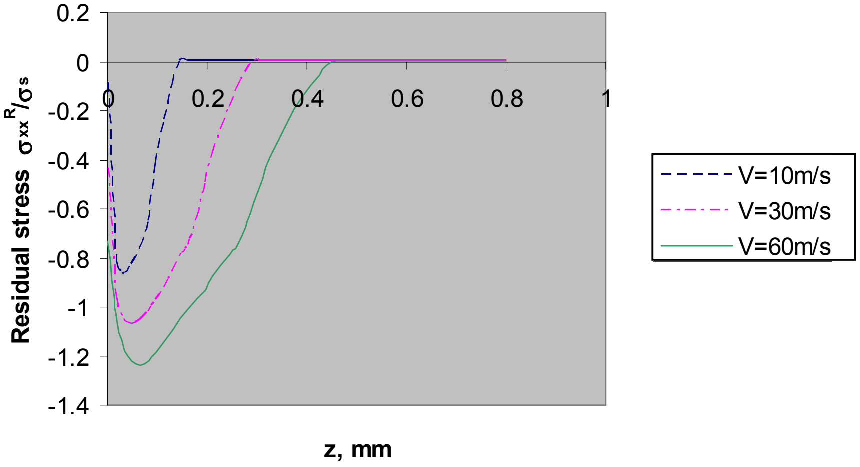

FIGURE 11. THE RESIDUAL STRESS DISTRIBUTION FOR SPECIMEN A1

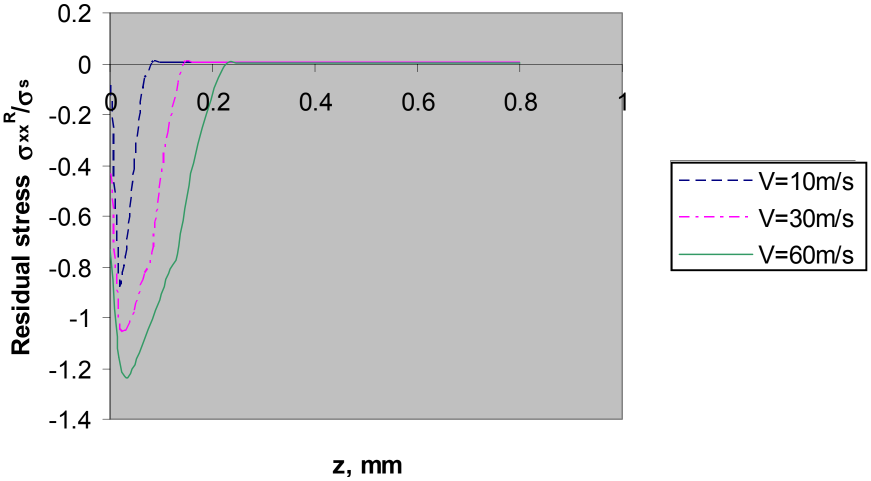

FIGURE 12. THE RESIDUAL STRESS DISTRIBUTION FOR SPECIMEN A2

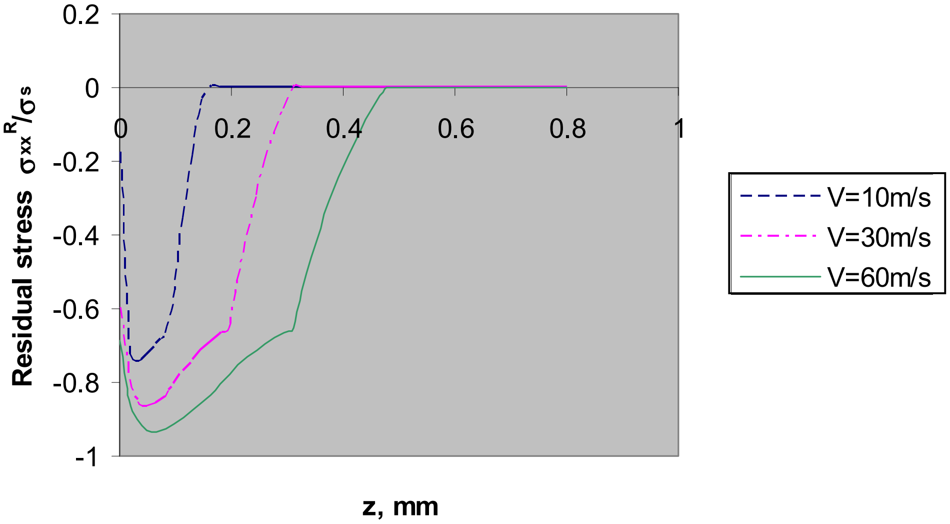

FIGURE 13. THE RESIDUAL STRESS DISTRIBUTION FOR SPECIMEN B1

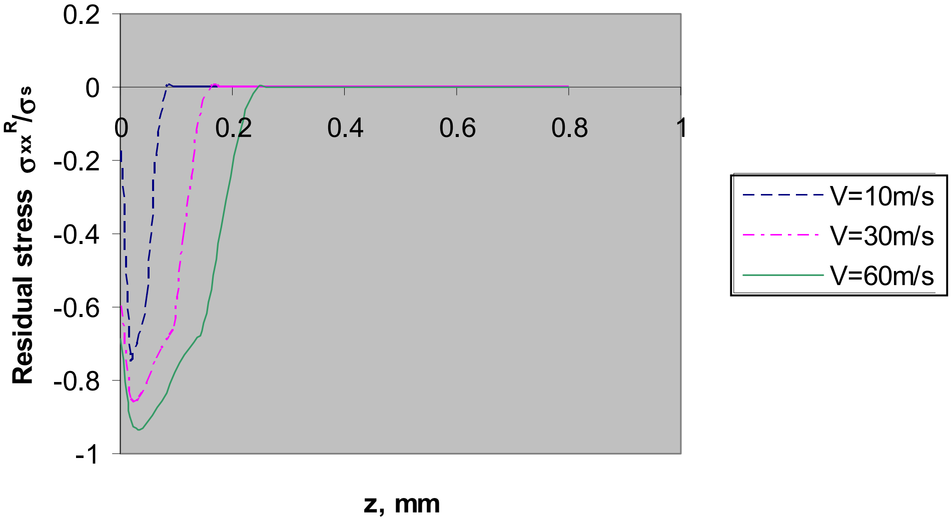

FIGURE 14. THE RESIDUAL STRESS DISTRIBUTION FOR SPECIMEN B2

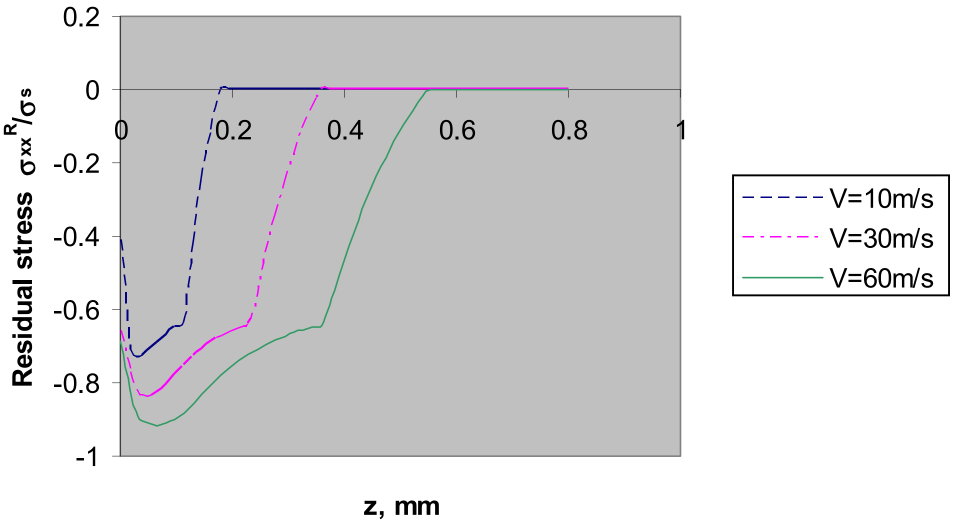

FIGURE 15. THE RESIDUAL STRESS DISTRIBUTION FOR SPECIMEN C1

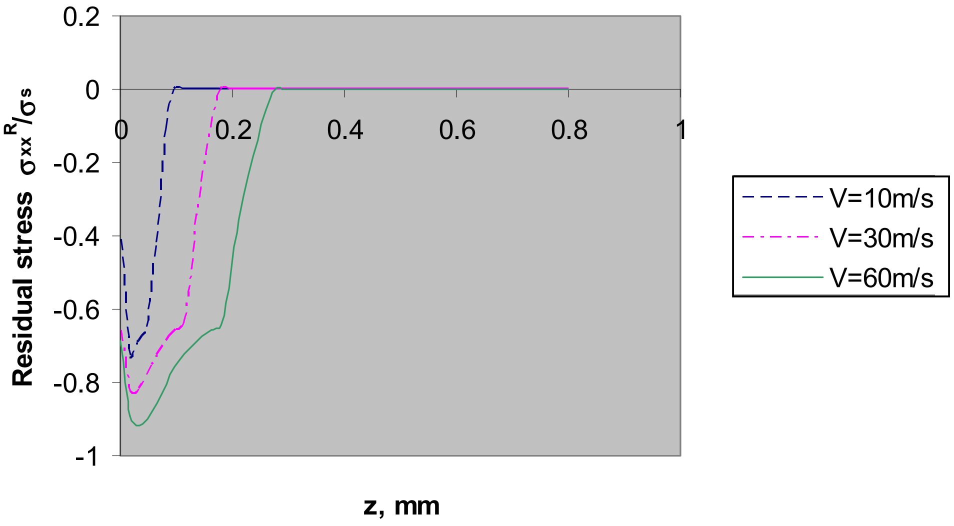

FIGURE 16. THE RESIDUAL STRESS DISTRIBUTION FOR SPECIMEN C2

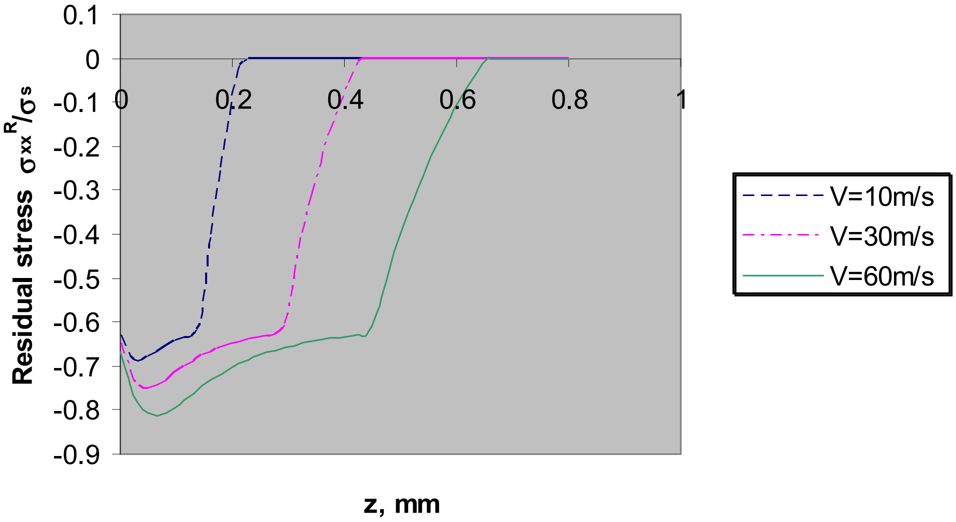

FIGURE 17. THE RESIDUAL STRESS DISTRIBUTION FOR SPECIMEN D1

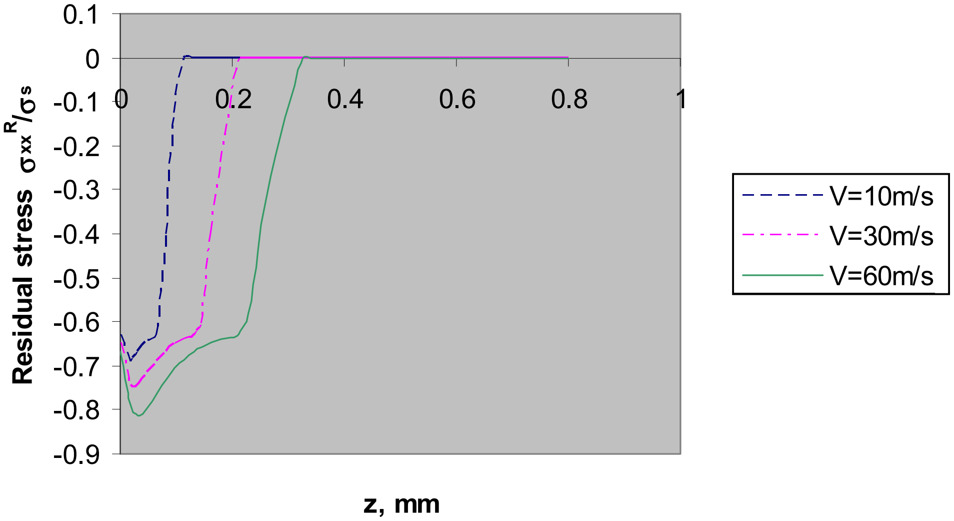

FIGURE 18. THE RESIDUAL STRESS DISTRIBUTION FOR SPECIMEN D2

The distribution of residual stress in 7075 aluminum was also considered. The material properties are given as follows:

$$E = 70\ GPa,\ v = 0.33,\ \sigma_s = 0.462\ GPa,\ \sigma_b = 0.526\ GPa,\ \varepsilon_b = 0.11,\ \rho = 2700\ kg/m^3$$

The distributions of the residual stress under different shot velocities for different radii of the shot are shown in figures 19 and 20.

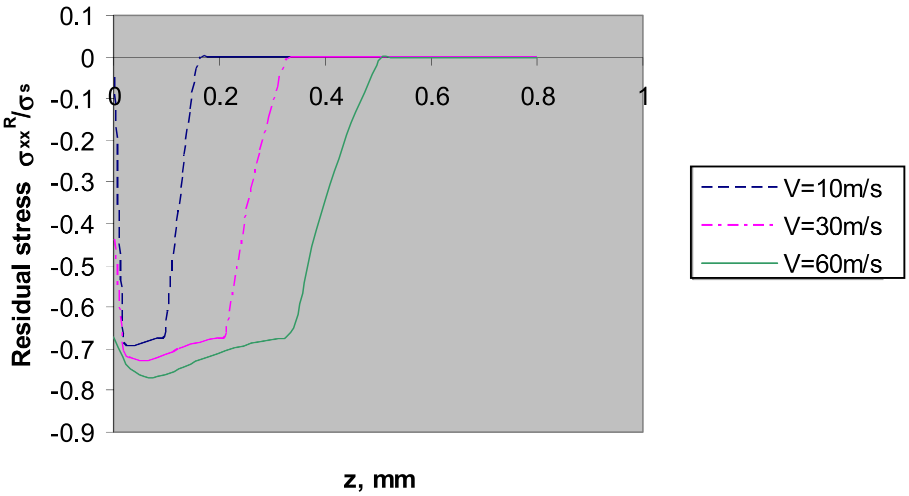

FIGURE 19. THE RESIDUAL STRESS DISTRIBUTION FOR 7075 ALUMINUM, *R* = 0.6 mm

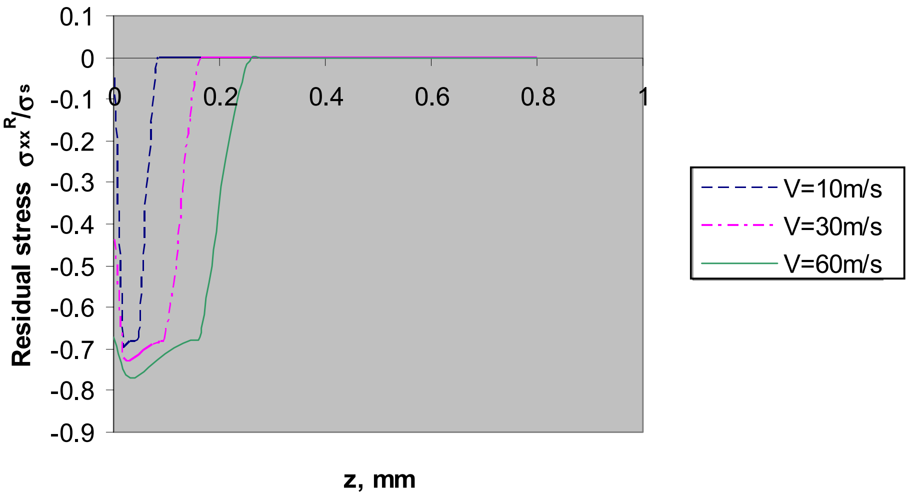

FIGURE 20. THE RESIDUAL STRESS DISTRIBUTION FOR 7075 ALUMINUM, *R* = 0.3 mm

It is seen that the predicted curves agree with the common trends found in the measured residual stress distributions (see figure 21 [5]).

The main parameters of the shot-peening process are found to be:

- radius *R* of the shot
- initial velocity *V* of the shot
- behavior of the material of sphere and of workpiece
- thickness of workpiece

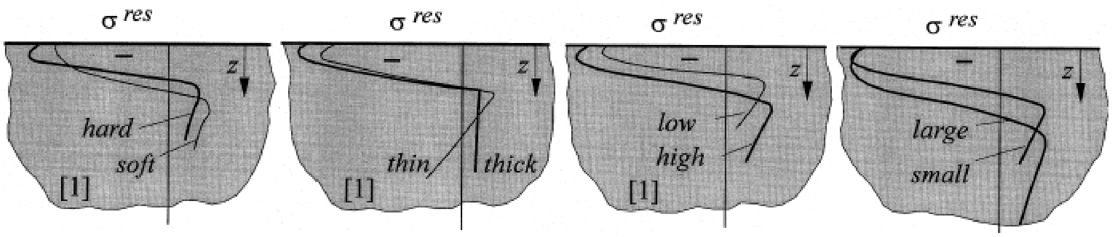

material of workpiece thickness of workpiece velocity of sphere radius of sphere

FIGURE 21. GENERAL INFLUENCE OF SHOT-PEENING PARAMETERS ON THE DISTRIBUTION OF RESIDUAL STRESSES

The general influence of these parameters on the distribution of the residual stresses obtained from experimental data is shown in figure 21. However, it should be noted that the present analysis model could not account for the effect of the thickness of the workpiece.

Figures 19 and 20 show that the larger radius sphere produced a larger compressive residual stress zone compared with the zone produced by smaller radius sphere, while the maximum value of the compressive residual stress was kept relatively constant. This trend was the same for all shot velocities.

Figures 11 through 20 also show that the higher the velocity of the sphere, the larger compressive residual stress zone and the maximum value of the compressive residual stress increased as the velocity of the sphere increased. For specimen D1, the influence of velocity of the sphere on the maximal value of the compressive residual stress is shown in figure 22. The influence of velocity of the sphere on the size of the compressive residual stress zone, i.e., the depth of the compressive residual stress layer in thickness direction (L_{CR}) is shown in figure 23.

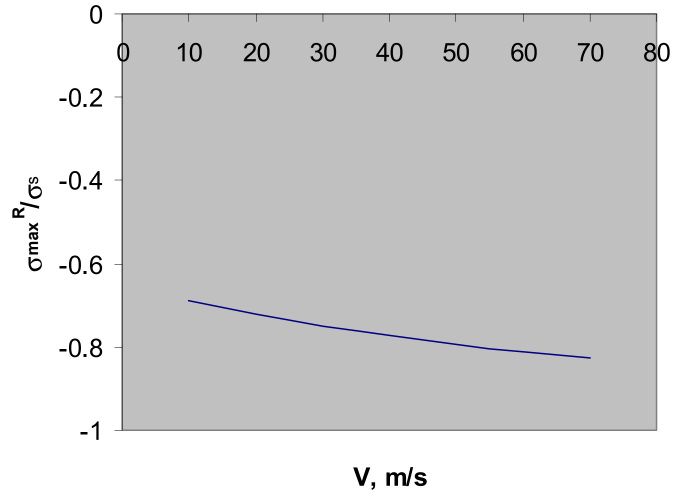

FIGURE 22. THE INFLUENCE OF THE VELOCITY OF THE SPHERE ON THE MAXIMAL VALUE OF THE COMPRESSIVE RESIDUAL STRESS

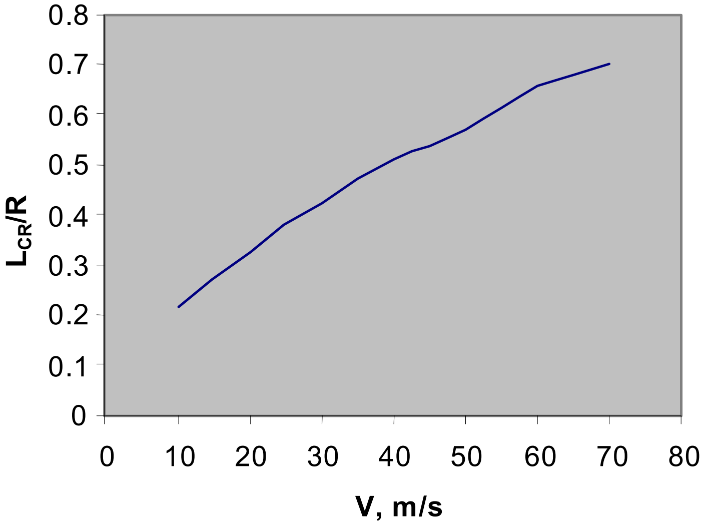

FIGURE 23. THE INFLUENCE OF THE VELOCITY OF THE SPHERE ON THE SIZE OF THE COMPRESSIVE RESIDUAL STRESS ZONE

The influence of the yield strength of the workpiece on the distribution of the residual stress is shown in figure 24; 40Cr steel was modeled with varying yield strength. It was found that the higher the yield strength of the workpiece, the smaller the compressive residual stress zone, and the maximum value of the compressive residual stress increased with increasing yield strength of the workpiece.

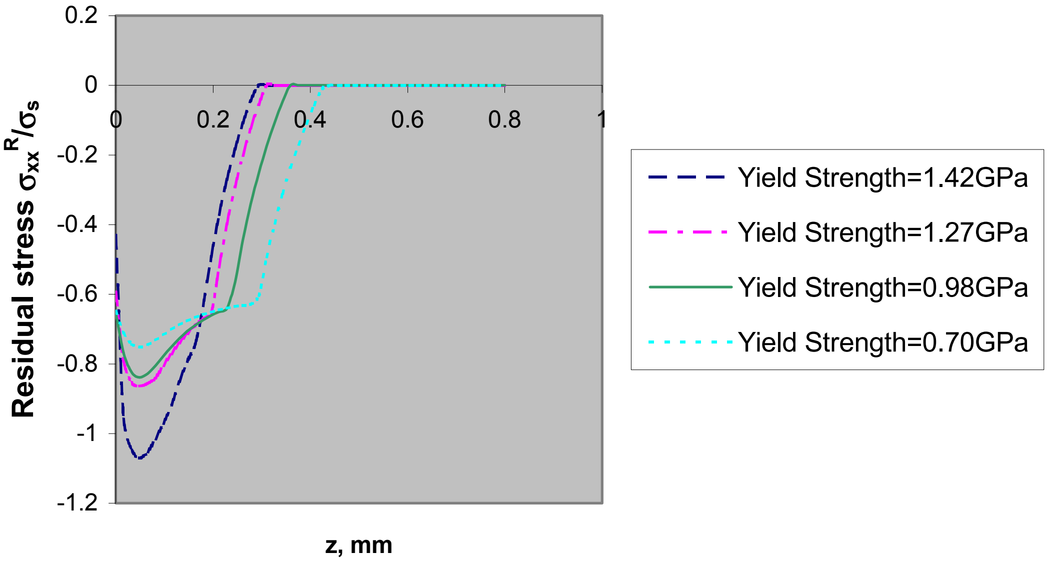

FIGURE 24. THE INFLUENCE OF THE YIELD STRENGTH OF THE WORKPIECE ON THE DISTRIBUTION OF THE RESIDUAL STRESS

These numerical results were instrumental in concluding that the newly developed analysis model is:

- Very simple and quick
- Effects of the velocity of the shot, diameter of the shot, and the material's characteristics are considered
- The material can be strain-hardening
- No empirical parameters are used

It should be pointed out that the current model could not give the tensile residual stress field, partly due to the assumption that the target material is semi-infinite.

The tensile residual stress field would appear, for finite thickness target material, as a result of the reflection of the stress waves. The tensile residual stress in finite-size (finite thickness as well as finite in-plane dimensions) specimens can be introduced by considering that the sum (integration) of residual stresses along the z axis should be zero.

5. MODELING FATIGUE CRACK GROWTH IN SHOT-PEENED STRUCTURAL COMPONENTS.

Since an approach to predicting the distribution of the residual stresses in a given workpiece has been accurately and efficiently developed, a discussion of the effect of the shot peening on the fatigue life of structural components will continue. It is well known that the shot-peening treatment of a material surface appreciably enhances the fatigue life of structural components. The presence of compressive residual stresses in the near-surface layer considerably extends the stage of short crack fatigue growth. It is worth noting that small fatigue crack growth stages are characterized for the dominant contribution to the overall life of structure. Experimental data of fatigue life extension for structural components made of steel and aluminum can be found, for example, in reference 20.

The effect of shot peening on crack growth is illustrated in figures 25 and 26. A 3D through crack with a straight initial crack front is considered. The crack front of an un-shot-peened workpiece is shown in figure 25 for the reported loading cycles. Analysis of a geometrically similar, but shot-peened, specimen produced the crack front shown in figure 26. As expected, it was demonstrated that the portion of the crack front, which is located within the compressive residual stress zone, propagates slower in comparison to the portion that lies outside of the compressive residual stress zone.

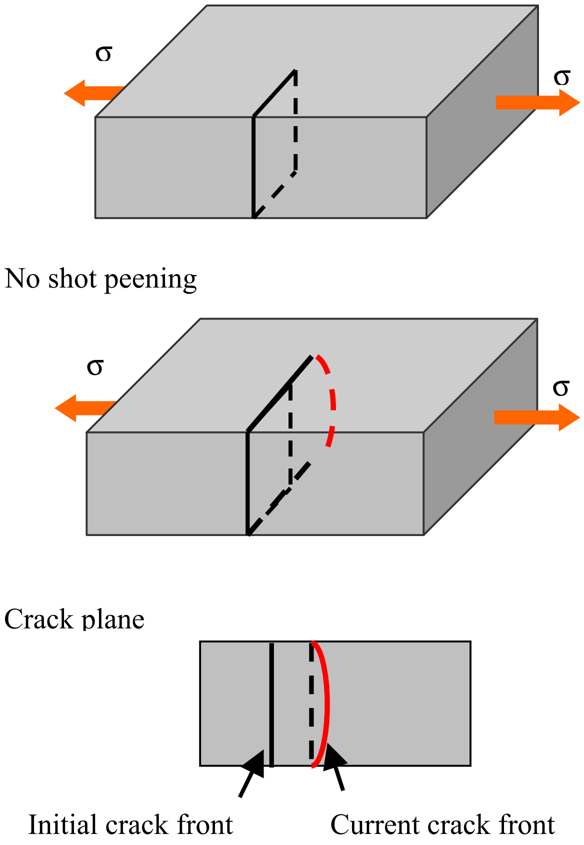
σ
σ
No shot peening
σ
σ
Crack plane
Initial crack front
Current crack front

FIGURE 25. CRACK GROWTH WITHOUT SHOT PEENING

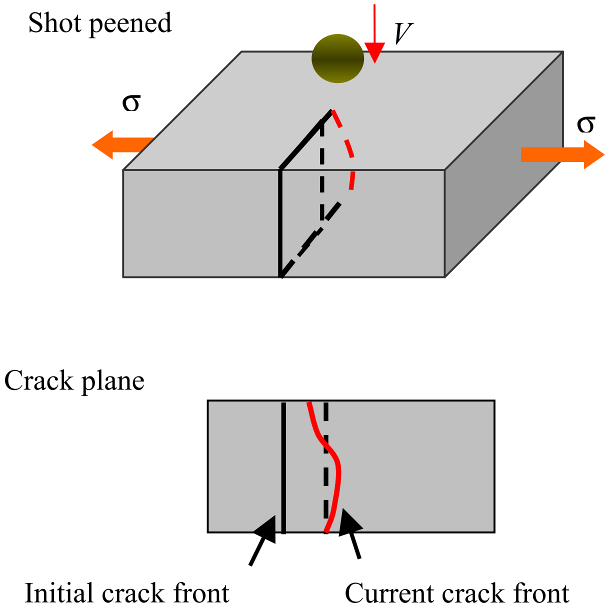
Shot peened
V
σ
σ
Crack plane
Initial crack front
Current crack front

FIGURE 26. CRACK GROWTH IN SHOT-PEENED STRUCTURAL COMPONENTS

Although it is currently difficult to expect that the direct numerical modeling of elastic-plastic fatigue growth of small cracks can produce practical results of sufficient accuracy, a practical approach to modeling fatigue crack growth in shot-peened structural components consists of (1) using an efficient numerical method for computing fracture mechanics parameters for the crack and (2) employing an approximate approach based on plastic strip model for predicting crack growth rates.

The finite element alternating method [26] is an efficient tool for calculating fracture mechanics parameters for cracks of complicated configurations. The crack is modeled by the Symmetric Galerkin Boundary Element Method as if it were in an infinite medium. The finite element method is independently used for the stress analysis of the uncracked structural component subjected to the applied loading. Proper superposition of two solutions is applied through the use of an iterative alternating procedure.

The following computational procedure was employed in this project for modeling small fatigue crack growth:

1. Calculate the stress-intensity factor range for a specified crack.

2. Using long crack data of the type $da/dN = C\Delta K^m$ predict $(da/dN)_1$, which takes into account elastic-plastic effects and residual stresses (using plastic strip model).

3. Perform integration for the number of cycles N, while crack advance is less than specified value.

4. Increment crack geometry and go to 1.

Based on the present analysis model of the shot peening, the effect of the shot peening on the fatigue life of structural components is investigated.

Consider a cracked specimen subjected to a constant-amplitude cyclic load (figure 27), the maximum stress intensity is $K_{\max}$ and the minimum is $K_{\min}$.

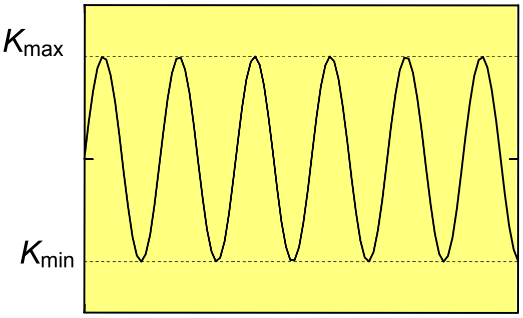

FIGURE 27. FATIGUE CRACK GROWTH

The stress-intensity factor range is

$$\Delta K = K_{\max} - K_{\min} \tag{37}$$

and the ratio of the stress is

$$R = \frac{K_{\min}}{K_{\max}} \tag{38}$$

The Paris' fatigue model follows

$$\frac{da}{aN} = C\left(\Delta K_{eff}\right)^n \tag{39}$$

as C and n are empirical material constants, the effective range of the stress-intensity factor ΔK_{eff} is defined as

$$\Delta K_{eff} = K_{\max} - K_{op} = (1-f)K_{\max} \tag{40}$$

Where K_{op} is the open (closure) stress-intensity factor at which the crack will open fully, and

$$f = \frac{K_{op}}{K_{\max}} \tag{41}$$

Many models that are fundamentally based on the Paris model were proposed by means of the Elber's crack closure concept.

Through the course of this project, three fatigue models were studied to determine the effects of shot peening on fatigue crack growth: the first is the modified NASGRO model; the second is the plastic strip model; and the third is the plastic zone model. These three methods were employed in this project and will be discussed in further detail.

5.1 MODIFICATION OF THE NASGRO MODEL.

Equation 42 is a modification of the NASGRO equation, as given in the NASGRO manual, developed by Forman and Newman at NASA, De Koning at National Aerospace Laboratory The Netherlands, and Henriksen at European Space Agency:

$$\frac{da}{dn} = C\left(\frac{1-f}{1-R}\right)^n \frac{\left(1-\Delta K_{th}/\Delta K\right)^p}{\left(1-K_{\max}/K_{crit}\right)^q} \tag{42}$$

Here, C, n, p, and q are empirical material constants; f depends on the ratio R. ΔK_{th} is the threshold value of ΔK; K_{crit} is the critical stress-intensity factor. Coefficient f is equal to

$$f = \frac{K_{op}}{K_{\max}} = \begin{cases} \max\left(R, A_0 + A_1 R + A_2 R^2 + A_3 R^3\right), & R \geq 0 \\ A_0 + A_1 R, & -2 \leq R < 0 \\ A_0 - 2A_1, & R < -2 \end{cases} \tag{43}$$

$$\begin{aligned} A_0 &= \left(0.825 - 0.3\alpha + 0.05\alpha^2\right)\left[\cos\left(\frac{\pi}{2}\frac{S_{\max}}{\sigma_0}\right)\right] \\ A_1 &= \left(0.415 - 0.071\alpha\right)\frac{S_{\max}}{\sigma_0} \\ A_2 &= 1 - A_0 - A_1 - A_3 \\ A_3 &= 2A_0 + A_1 - 1 \end{aligned} \tag{44}$$

Where α is the plane stress/strain constraint factor and $S_{\max}/\sigma_0$ is the ratio of the maximum applied stress to the flow stress. Here, the flow stress is the mean of the yield stress and the ultimate tension strength. The threshold stress-intensity range is given by

$$\Delta K_{th} = \Delta K_0 \left(\frac{a}{a + a_0}\right)^{1/2} \Bigg/ \left(\frac{1 - f}{\left(1 - A_0\right)\left(1 - R\right)}\right)^{\left(1 + C_{th} R\right)} \tag{45}$$

where ΔK_0 is the threshold stress-intensity range at $R = 0$; a is the crack length (depth of surface size); a_0 is the intrinsic crack length (0.0015 inches or 0.0381 mm); C_{th} is the threshold coefficient. The thickness effect is taken into account using the critical stress-intensity factor K_{crit}.

$$K_{crit} / K_{IC} = 1 + B_k \exp\left[-\left(A_k \frac{t}{t_0}\right)^2\right] \tag{46}$$

Here K_{IC} is Mode I plane strain fracture toughness; A_k and B_k are the fit parameters; t is the thickness; t_0 is the reference thickness (plane strain conditions). The reference thickness is determined by the equation

$$t_0 = 2.5\left(\frac{K_{IC}}{\sigma_{yc}}\right)^2 \tag{47}$$

Equation 42 can be rewritten as

$$\frac{da}{dn} = C\left(\Delta K_{eff}\right)^n \frac{\left(1-\Delta K_{th}/\Delta K\right)^p}{\left(1-K_{\max}/K_{crit}\right)^q} \tag{48}$$

When no shot peening effects are involved, the effective range of the stress-intensity factor can also be written as

$$\Delta K_{eff} = \frac{S_{\max} - S_{op}}{S_{\max} - S_{\min}} \Delta K \tag{49}$$

where $S_{\min}$ is the minimum applied stress, and S_{op} is the crack opening stress. The stress-intensity factor range is

$$\Delta K = \left(S_{\max} - S_{\min}\right)\sqrt{\pi a}\, f(a) \tag{50}$$

Now, if one considers the effects of the shot peening, the maximum and minimum stress will decrease or increase due to the residual stresses from shot peening, as shown in figure 28.

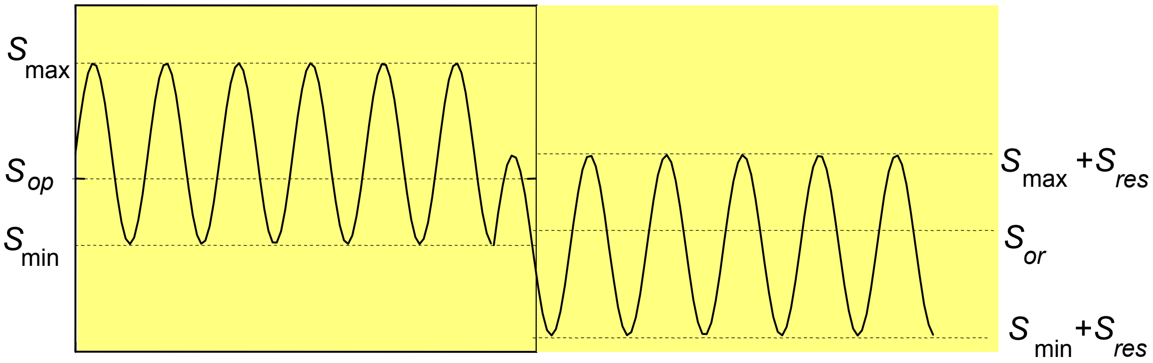

FIGURE 28. THE EFFECT OF THE RESIDUAL STRESS

Thus, the effective stress can be obtained as

$$\Delta S_{eff} = \left(S_{\max} + S_{res}\right) - S_{or} \tag{51}$$

and the effective stress-intensity factor range can be written as

$$\Delta K_{eff} = \Delta S_{eff} \sqrt{\pi a}\, f(a) \tag{52}$$

Here, S_{or} is calculated by adding the compressive residual stress S_{res} to the applied minimum and maximum stress, the new minimum ($S_{\min} + S_{res}$) and maximum stress ($S_{\max} + S_{res}$) are then used in the crack closure model to calculate the opening stress. Thus, the ratio is modified as

$$R = \frac{S_{\min} + S_{res}}{S_{\max} + S_{res}} \tag{53}$$

Then by using the new maximum stress ($S_{\max} + S_{res}$) and minimum stress ($S_{\min} + S_{res}$), from equation 43, one can obtain the new open stress S_{or}.

The modified NASGRO model is inherently simple, and conveniently takes the effect of the compressive residual stresses due to shot peening, via a slight modification of the existing code.

The original NASGRO model will be used to demonstrate the effect of the shot-peening consideration to the crack growth. The stable crack growth in the 2024-T351 single-edged notch bend (SENB) specimens was initially considered, without shot peening. Limited three-point bend fatigue testing of 8.1-mm-thick 2024-T351 aluminum alloy, SENB were conducted by Prof. Kobayashi at the University of Washington. All specimens were tested in the as-received condition with crack faces perpendicular to the rolling direction, i.e., in the L-T direction. The SENB specimens, as shown in figure 29, were machined from an 8.1-mm-thick 2024-T3 aluminum stock plate.

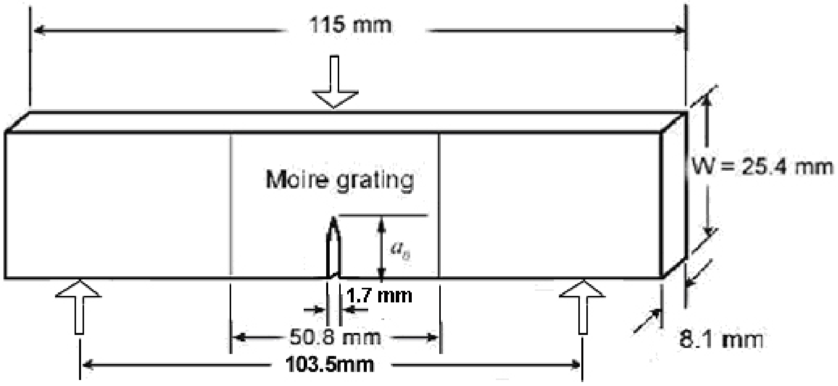

a_0 =13 mm

FIGURE 29. THE SENB SPECIMEN

Uniaxial tension tests were performed on the subsized tensile coupons, and three-point bending fatigue testing were performed on the SENB specimens using an Instron Model 8511 test system with a 3000-lb load cell. Due to the lack of compression grips on this testing system, the compressive stress-strain relations were not obtained. The crack in a SENB specimen was fractured after a given fatigue cycle. The cracked cross sections were observed and recorded by a charge-coupled device camera. The digitized picture was used to measure the crack-tunneling profile. Three 2024-T351 SENB specimens were fatigued to different cycles. Figure 30 shows a typical crack growth profile of an as-received 2024-T351 SENB specimen that was fatigued to 8403 cycles. Table 1 shows the load and crack profiles of the three specimens. The crack profiles of all three fatigues specimens were effectively identical with typical retardation of the crack profile along two surfaces, as shown in figure 30. Specimen A4 fractured at 10,392 cycles and yielded a fracture toughness of 38 MPa√m, which is close to the handbook value of 34 MPa√m [11]. Figure 31 shows the measured crack profiles of the top and bottom faces for the three specimens. The maximum plane strain, plastic zone size under monotonic loading is estimated to be 0.8 mm at fracture. The negligible plastic zone size did not justify Moiré interferometry analysis to obtain the elastic displacement and strain fields of the SENB specimen.

TABLE 1. FATIGUE CRACK PROFILE OF AS-RECEIVED 2024-T351 SENB SPECIMENS, $R = 0.1$

Test A2			
P_{max} (kN)	P_{min} (kN)	Cycles	
1.725	0.173	4963	
Top		Bottom	
X (mm)	Y (mm)	X (mm)	Y (mm)
0.84	0.09	0.51	0.27
2.10	2.10	2.05	2.10
2.10	4.20	2.05	4.20
2.10	6.30	2.15	6.30
1.45	8.08	0.62	8.01
Test A3			
P_{max} (kN)	P_{min} (kN)	Cycles	
1.699	0.233	8402	
Top		Bottom	
X (mm)	Y (mm)	X (mm)	Y (mm)
3.55	0.07	3.57	0.09
4.22	2.10	4.15	2.10
4.22	4.20	4.14	4.20
4.10	6.30	4.21	6.30
3.60	8.01	3.68	8.08
Test A4			
P_{max} (kN)	P_{min} (kN)	Cycles	
1.691	0.229	10392	
Top		Bottom	
X (mm)	Y (mm)	X (mm)	Y (mm)
5.13	0.02	5.17	0.11
5.67	2.10	5.55	2.10
6.07	4.20	5.70	4.20
6.15	6.30	5.72	6.30
5.49	8.06	5.32	8.06

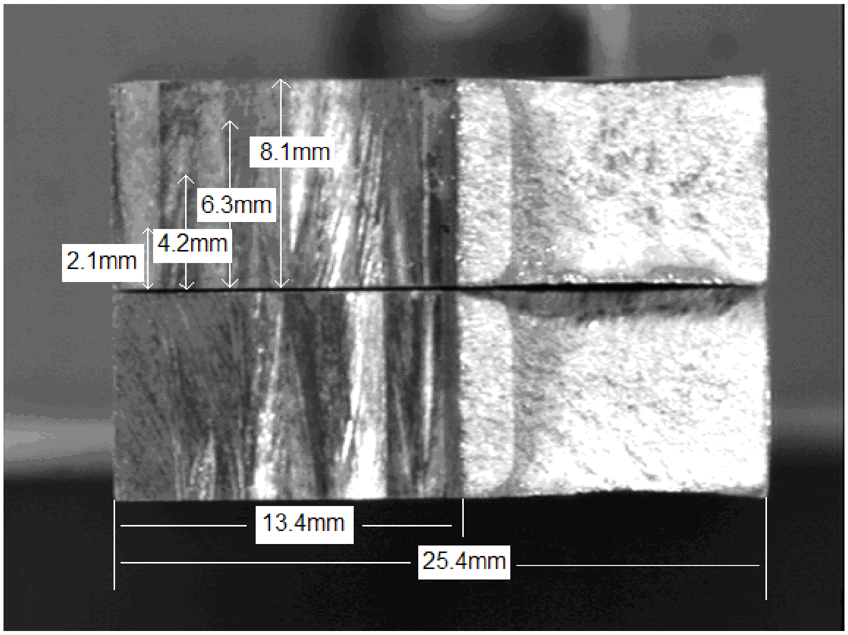
8.1mm
6.3mm
4.2mm
2.1mm
13.4mm
25.4mm

FIGURE 30. CRACK-TUNNELING PROFILE OF A FATIGUED 2024-T351 SENB SPECIMEN, SPECIMEN A3

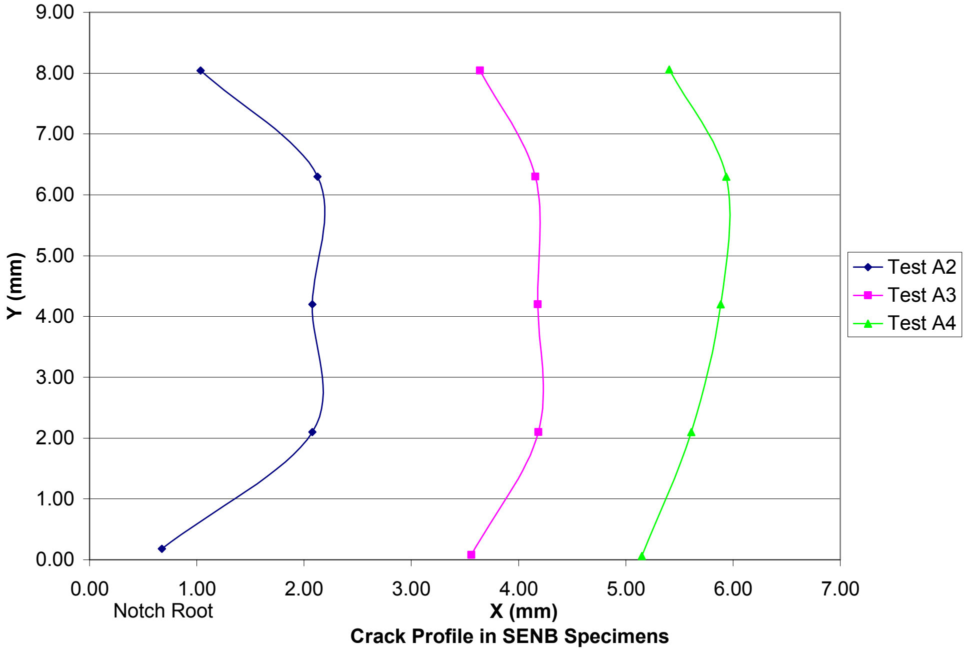

FIGURE 31. MEASURED CRACK PROFILES OF THREE FATIGUED AS-RECEIVED 2024-T351 SENB SPECIMENS

AGILE 3D and the modified NASGRO model were employed to simulate these tests. The global model of the specimen consisted of 960, 20-noded hexahedral elements, as shown in figure 32. The boundary element method (BEM) model of the crack plane with 12 eight-noded quadrilateral elements along the crack front is shown in figure 33.

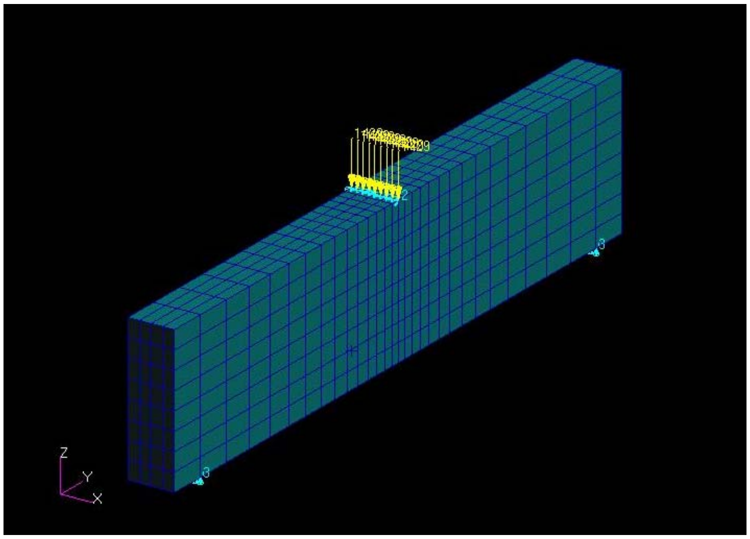

FIGURE 32. THE GLOBAL FEM MODEL

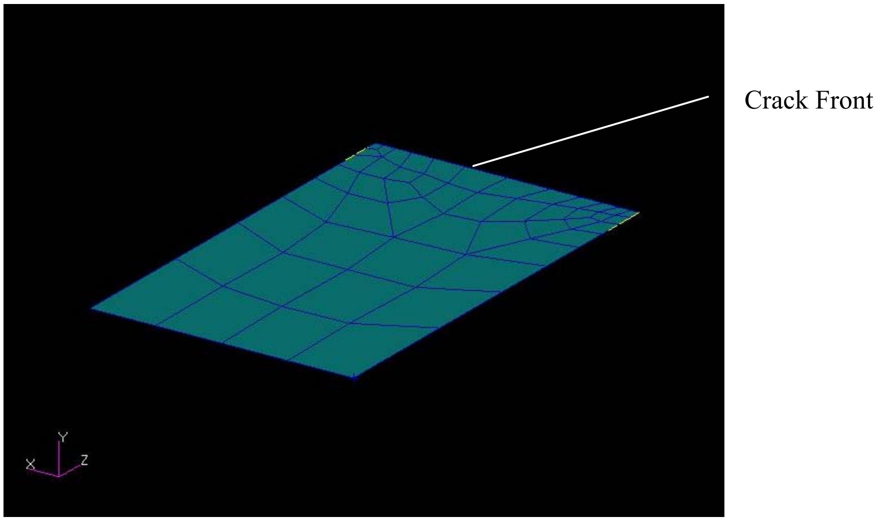

FIGURE 33. THE BEM MODEL IN THE CRACK PLANE

The numerical results for the crack-tunneling profiles are shown in figures 34 through 36 for tests A2 through A4, respectively. Comparison between the numerical and experimental results for the crack profiles of the three specimens is shown in figure 37. In examining these figures, it is verified that AGILE 3D accurately and efficiently simulates crack propagation of through cracks.

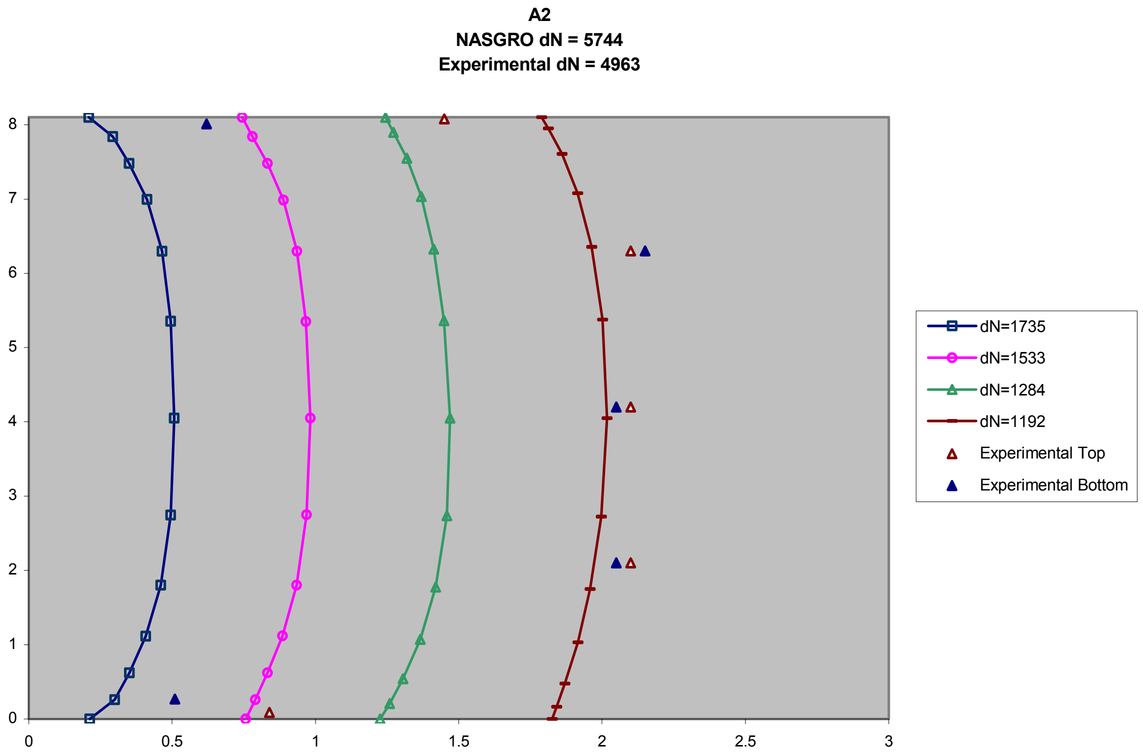

FIGURE 34. CRACK PROFILES FOR TEST A2

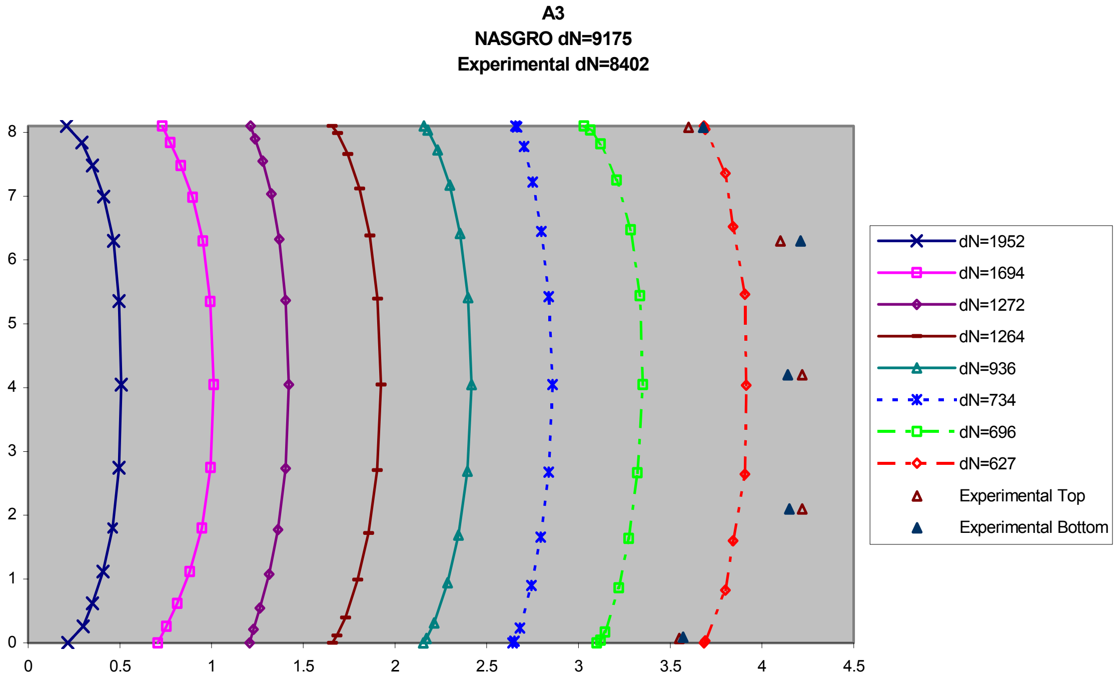

FIGURE 35. CRACK PROFILES FOR TEST A3

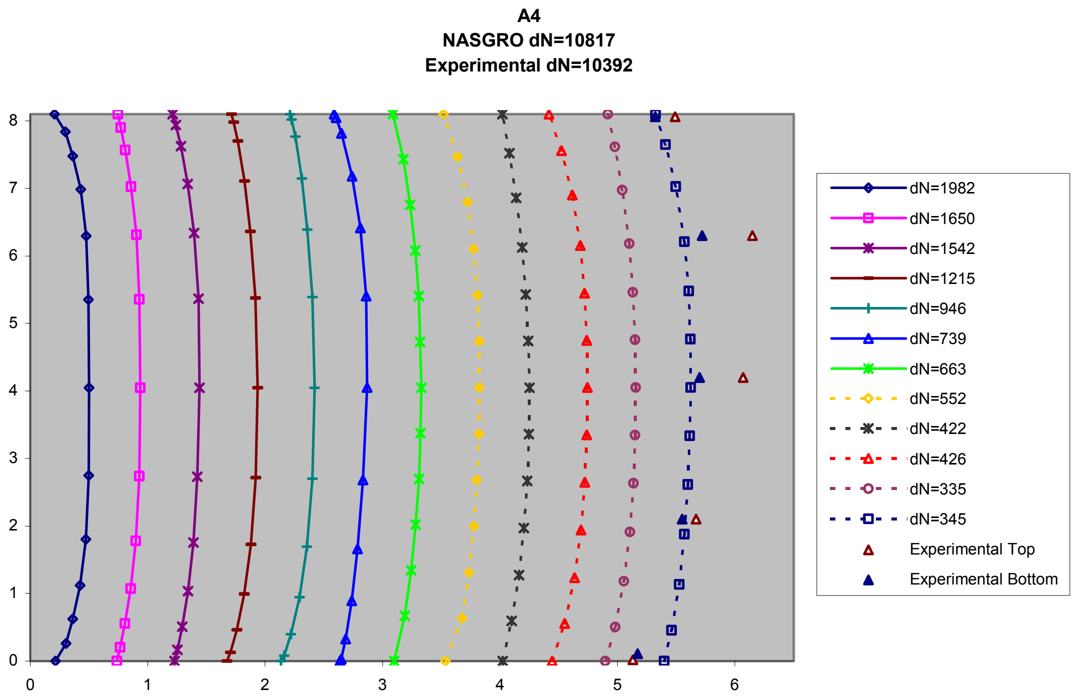

FIGURE 36. CRACK PROFILES FOR TEST A4

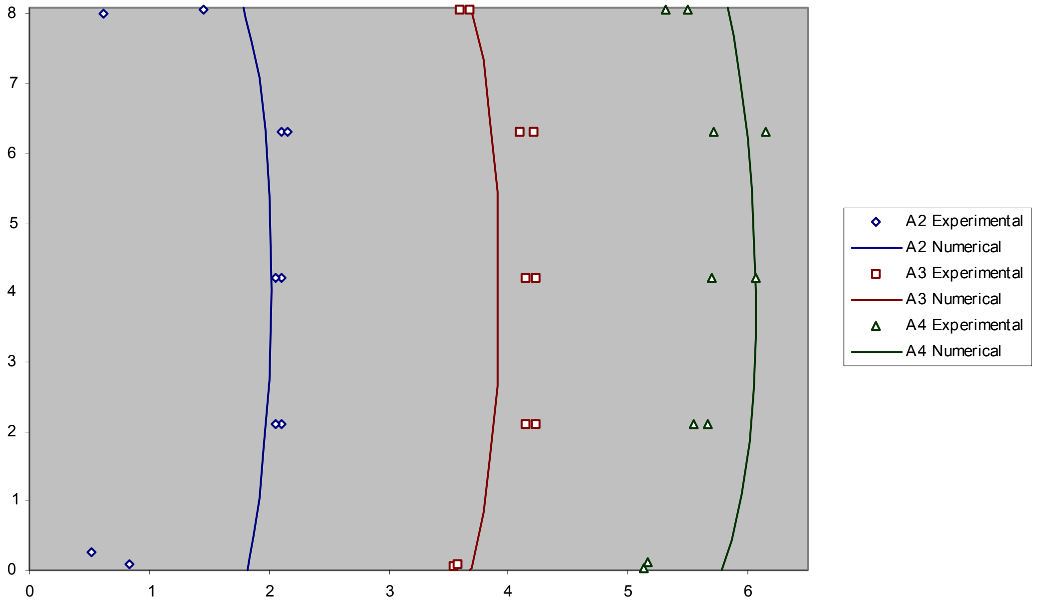

FIGURE 37. THE COMPARISON BETWEEN NUMERICAL AND EXPERIMENTAL RESULTS FOR THE CRACK PROFILES

The effect of the residual compressive stress field on crack propagation was performed via an analysis of a shot-peened workpiece. Tension/tension fatigue crack growth in 1.8-mm-thick 7075-T7351 aluminum plate, double-edged notch specimens, as in figure 38, is considered.

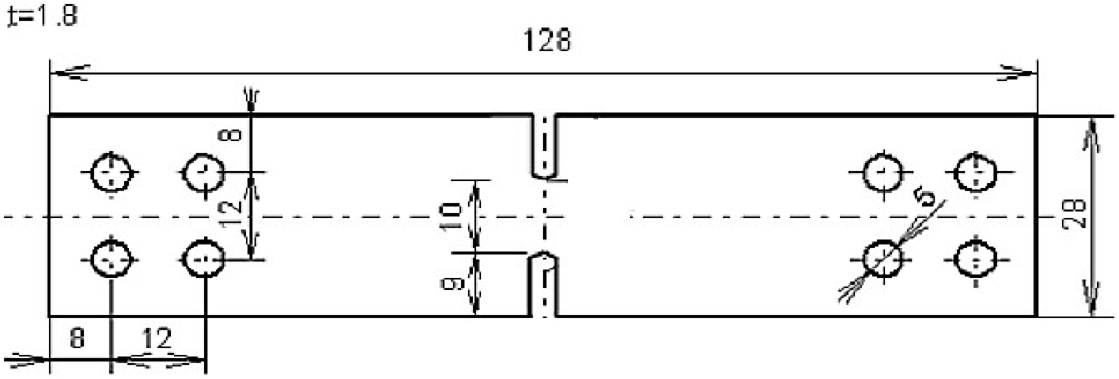

FIGURE 38. DOUBLE-EDGED NOTCH SPECIMEN

A maximum tension of 400 lbs with a ratio of *R* = 0 was applied to demonstrate the effect of the shot peening on the crack propagation profile. Both shot-peened and un-shot-peened specimens were analyzed. The shot-peened specimen was peened under the following condition:

- Intensity 0.017A, shot size 230-280, coverage 1.0

The specimen was only shot peened on one side. The residual stress distribution shown in figure 39 was found by means of the theoretical model developed in section 3.

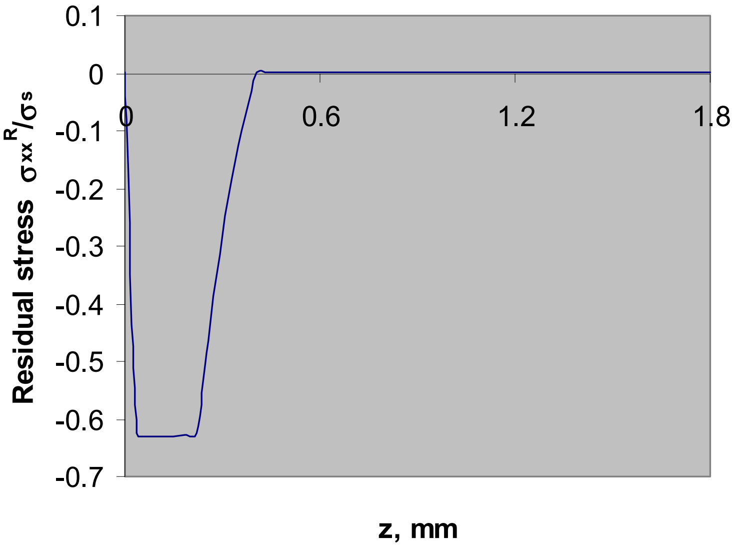

FIGURE 39. THE RESIDUAL STRESS DISTRIBUTION FOR 7075 ALUMINUM

Since a target material of finite thickness is now being considered, it is possible to determine the tensile residual stress field that is due to the reflection of the stress waves. The tensile residual stresses are found by the following simple approach:

- Integration of the compressive stress through the thickness
- Determination of the average compressive stress
- Sign reversal (to tension)
- The addition of the average tensile stress to the actual compressive stress through the thickness

AGILE 3D and the modified NASGRO model are employed to simulate the effects due to the shot-peening process. The residual stresses due to shot peening are incorporated in the AGILE 3D model easily by only modifying the maximum and minimum loading by S_{res}, which is derived from the analytical model through equations 51-53. In these examples, one does not consider the residual redistribution during the crack growth. Only half of the specimen is modeled due to the inherent symmetry of the problem. The global model with 40, 20-noded hexahedral elements is shown in figure 40. The BEM model with six, eight-noded quadrilateral elements along the crack front is shown in figure 41.

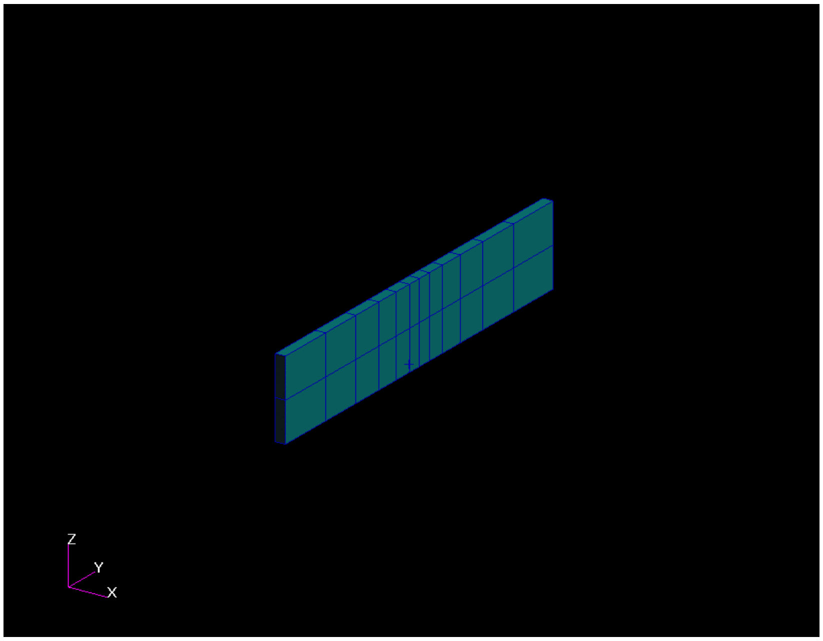

FIGURE 40. THE GLOBAL FEM MODEL

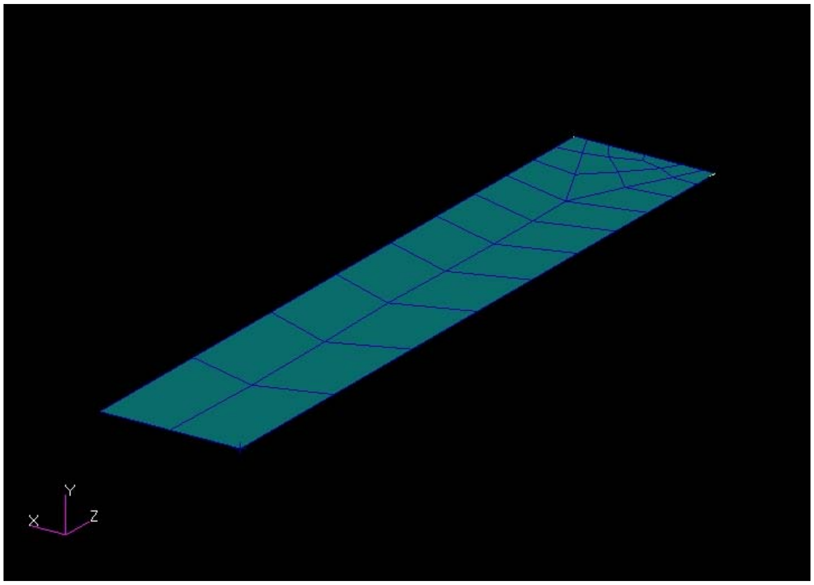

FIGURE 41. THE BEM MODEL IN THE CRACK PLANE

The fatigue crack profiles of the shot-peened and non-shot-peened specimens generated through AGILE 3D analyses are shown in figure 42. It was observed that the peened surface was found to retard crack propagation. Figure 43 depicts the effect of the peening on the fatigue crack growth because the crack grows slower in the shot-peened specimen and especially slow on the surface of the shot-peened specimen.

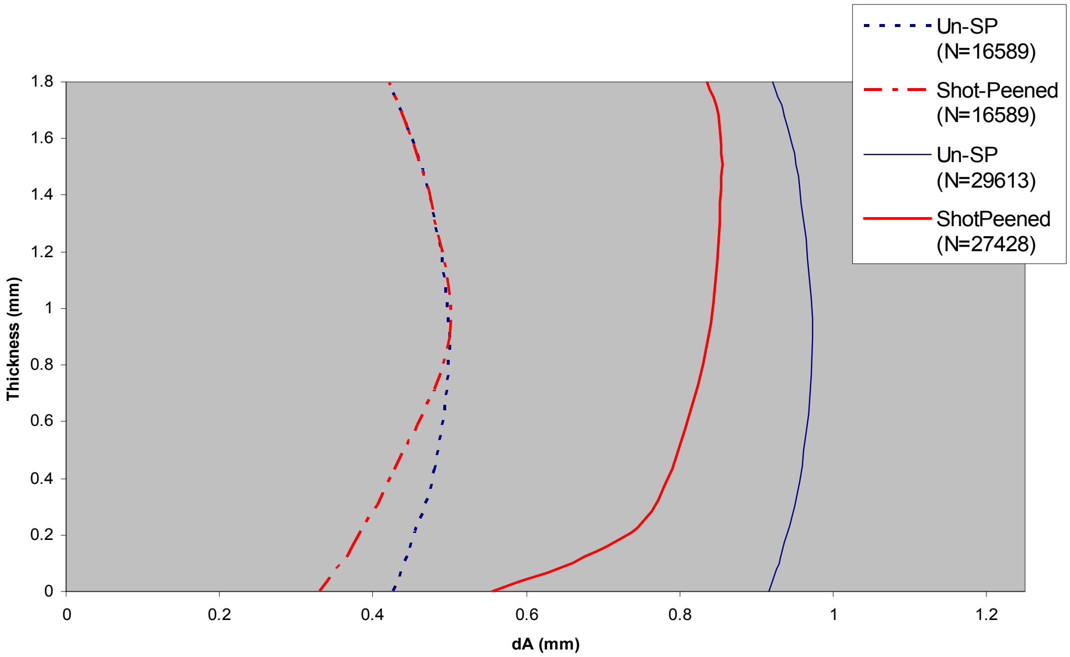

FIGURE 42. THE CRACK PROFILES FOR SHOT-PEENED AND NOT SHOT-PEENED SPECIMENS

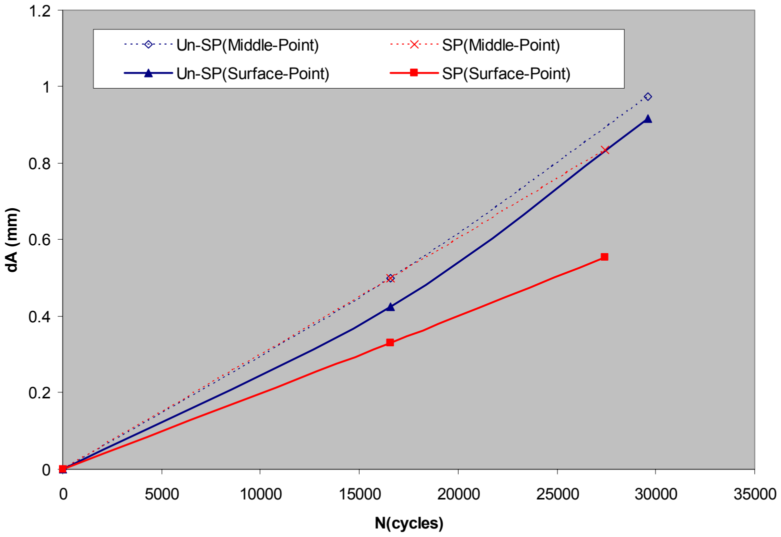

FIGURE 43. THE EFFECT OF SHOT PEENING ON CRACK GROWTH

5.2 PLASTIC STRIP MODEL.

The application of plastic strip models for small fatigue crack growth modeling is considered in references 25 and 27. According to the plastic strip model (figure 44), near-tip plastic yielding is assumed to be localized in thin strips near the crack tips. These plastic strips are modeled as additional discontinuities to satisfy plasticity conditions. The rest of the body is considered elastic. In reference 25, the plastic strip model is combined with a method of singular integral equations for predicting growth of small fatigue cracks. In reference 27, the plastic strip model is extended to incorporate the effects of shot peening. The crack is divided into three zones: the crack, the plastic zone, and the barrier zone (grain boundary). The extended plastic strip model can take into account both effects of residual stresses and material microstructure, which can be affected by the shot-peening process.

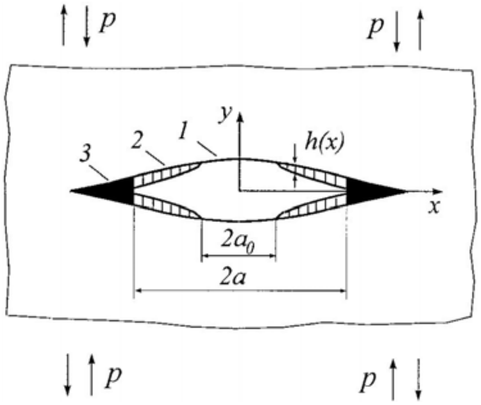

FIGURE 44. PLASTIC STRIP MODEL FOR A CRACK (1) INITIAL CRACK, (2) PLASTIC STRETCH, AND (3) PLASTIC ZONE
(The effects of the shot peening are considered in zones 1 and 2.)

The residual stress due to shot peening is introduced as a material variable (resistance to crack opening) rather than superimposing it linearly with the applied stress.

Consider a crack of length $2a$ in a plate subjected to cyclic loading ($S_{\min} \leq S \leq S_{\max}$). The residual stresses on the crack edges are due to shot peening. The crack edges are modeled via the residual stresses at the cycle's maximum loading conditions. The plastic zone is then modeled by the strip model, where the boundary normal stresses are equal to the yield strength of the material.

$$\begin{aligned} \sigma_y(x) &= \sigma^R(z), & |x| < a \\ \sigma_y(x) &= \alpha\sigma_0, & a < |x| < c \end{aligned} \tag{54}$$

where α is the plastic constraint factor, account for the 3D effect during plastic yielding near the crack tip. $\alpha = 1$ corresponds to the plane stress, while $\alpha = 3$ corresponds to the plane strain. Since these two extreme cases are rarely realized in their pure forms, accurate conditions are modeled by intermediate values ranging between $1 < \alpha < 3$. The material ahead of the crack is assumed to deform plastically if the tensile stresses reach a value of $\alpha\sigma_0$, and the compressive plastic yielding begins at $-\sigma_0$. σ^R is denoted as the compressive residual stress due to shot peening or cold-working. Parameters a and c are illustrated in figure 45.

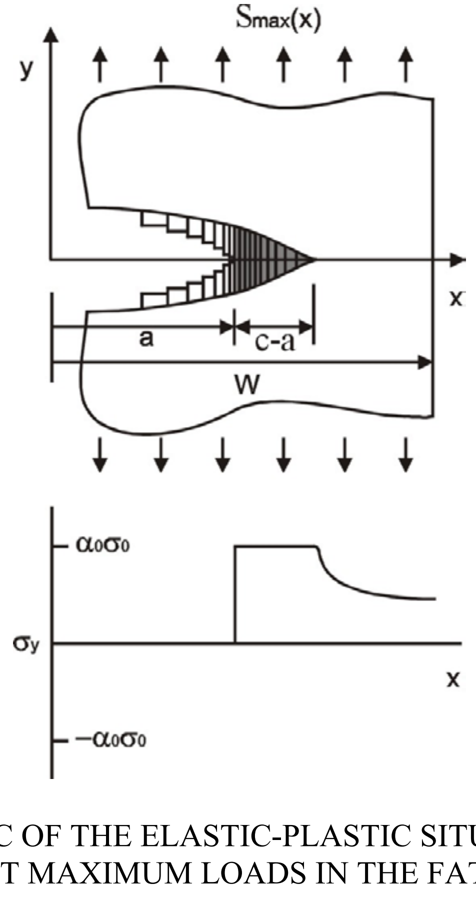

FIGURE 45. SCHEMATIC OF THE ELASTIC-PLASTIC SITUATION NEAR FATIGUE CRACK TIP AT MAXIMUM LOADS IN THE FATIGUE CYCLE

During unloading, reverse plastic yielding occurs in the vicinity of the crack tip in the cyclic plastic zone. Within this zone the local stresses are equal to the compressive yield strength of the material.

$$\begin{aligned} &\sigma_y(x) = \sigma_y^R(z), && |x| < b \\ &u_{\min}(x) = h(x), && b < |x| < a \\ &\sigma_y(x) = -\sigma_0\,, && a < |x| < d \\ &u_{\min}(x) = u_{\max}(x), && d < |x| < c \end{aligned} \tag{55}$$

where $u_{\max}(x)$ and $u_{\min}(x)$ are normal displacements of the crack surfaces at the maximum and minimum loads, respectively. $h(x)$ is the thickness of the plastic strip on the fatigue crack surfaces. Parameters *a, b, d,* and *c* are illustrated in figure 46.

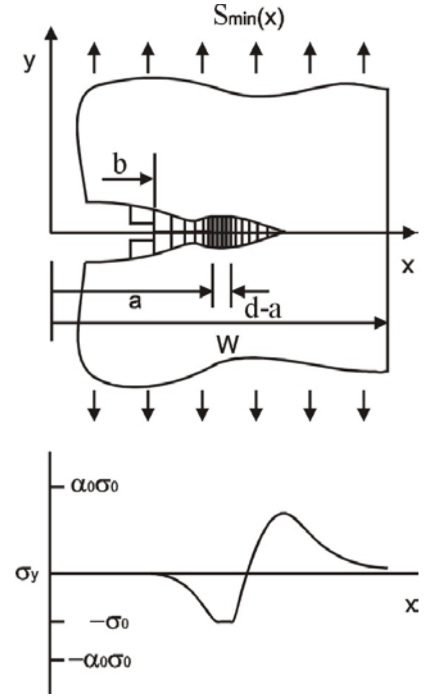

FIGURE 46. SCHEMATIC OF THE ELASTIC-PLASTIC SITUATION NEAR FATIGUE CRACK TIP AT MINIMUM LOADS IN THE FATIGUE CYCLE

Let the crack and plastic zones be represented by an array of continuous dislocations. The density of which can be determined by satisfying the prescribed boundary and single-value conditions. Based on the dislocation theory, the distribution of edge dislocations at any point within the crack and plastic zone subjected to the applied, frictional stresses, and residual stresses can be written for equilibrium as

$$-\frac{E}{4\pi(1-v^2)}\int_{-c}^{c}\frac{F(t)}{x-t}dt = P(x) \quad -c<x<c \tag{56}$$

Where E is the Young's modulus, v is the Poisson ratio, $F(t)$ is the dislocation density at any point along x axis. The resultant stress $P(x)$ is a function of x coordinate, depending on the applied, residual, and friction stresses that may vary from region to region. $P(x)$ can be written as

$$P(x) = \begin{cases} S_{\max} - \sigma^R & |x| \le a \\ S_{\max} - \alpha\sigma_0 & a < |x| < c \end{cases} \tag{57}$$

The dislocation density can be defined as

$$F(x) = \frac{d\delta(x)}{dx} = 2\frac{du(x)}{dx} \tag{58}$$

Here $\delta(x)$ is the crack opening displacement.

The general solution bounded at $x = \pm c$ for the dislocation density function is given by [28]

$$F(x) = \frac{(1-v^2)(\alpha\sigma_0 - \sigma^R)}{4\pi E}[\omega(x,a,c) - \omega(-x,a,c)] \tag{59}$$

where

$$\omega(x,a,c) = \cosh^{-1}\left|\frac{c^2 - ax}{c(a-x)}\right| \tag{60}$$

A condition in which the dislocation density function must be equal to zero at the end of the plastic zone to maintain continuity across the boundary was adopted. This condition also leads to the following formula for determining the plastic zone size.

$$\frac{a}{c} = \sin\left(\frac{\pi}{2}\frac{\alpha\sigma_0 - S_{\max}}{\alpha\sigma_0 - \sigma^R}\right) \tag{61}$$

The crack tip opening displacement (CTOD) can be evaluated as

$$\delta_{\max} = 2u_{\max}(a) = \frac{8a(1-v^2)(\alpha\sigma_0 - \sigma^R)}{\pi E}\ln\left(\frac{c}{a}\right) \tag{62}$$

The analysis is more complicated at minimum loading, in part because of the distribution of contact stresses, $\sigma_{con}(x)$, that act on the closed part of the crack is unknown. To find this distribution, a problem with the condition in equation 55, but with the second equality replaced by

$$\sigma_y(x) = -\sigma_{con}(x) + \sigma^R \quad b < |x| < a \tag{63}$$

The boundary condition corresponding to the function $\Delta u(x) = u_{\max}(x) - u_{\min}(x)$, which is displacement of the crack surfaces on passing from the maximum to minimum loads in the cycle, can be written as

$$\begin{aligned} &\sigma_y(x) = 0, && |x| < b \\ &\sigma_y(x) = \sigma_{con}(x), && b < |x| < a \\ &\sigma_y(x) = (1+\alpha)\sigma_0, && a < |x| < d \end{aligned} \tag{64}$$

for external stresses $(S_{\min} - S_{\max})$.

Similar to that in the maximum load, based on the dislocation theory, the equilibrium equation can be written as

$$-\frac{E}{4\pi(1-v^2)}\int_{-d}^{d}\frac{f(t)}{x-t}dt = P(x) \quad -d<x<d \tag{65}$$

where the dislocation density function $f(x)$ is defined as

$$f(x) = 2\frac{d\Delta u(x)}{dx} \tag{66}$$

and the resultant stress $P(x)$ can be written as

$$P(x) = \begin{cases} S & |x| \le b \\ S - \sigma_{con}(\mathrm{x}) & b < |x| < a \\ S - (1+\alpha)\sigma_0 & a < |x| < d \end{cases} \tag{67}$$

Here

$$S = S_{\max} - S_{\min} \tag{68}$$

For $b < |x| < a$, it can be obtain that

$$\frac{du_{\min}(x)}{dx} = \frac{dh(x)}{dx} \tag{69}$$

Then, from equations 65 and 69, an integral equation can be derived to estimate the contact stress $\sigma_{con}(x)$.

$$\int_b^a \frac{\sigma_{con}(t)dt}{\sqrt{d^2-t^2}\left(x^2-t^2\right)} = \frac{\pi E}{4\left(1-\nu^2\right)x\sqrt{d^2-x^2}} H(x) \tag{70}$$

with

$$\begin{aligned} H(x) = & \frac{dh(x)}{dx} - \frac{2\left(1-\nu^2\right)\left(\alpha\sigma_0-\sigma^R\right)}{\pi E}\left[\omega(x,a,c)-\omega(-x,a,c)\right] \\ & + \frac{2\left(1-\nu^2\right)(1+\alpha)\sigma_0}{\pi E}\left[\omega(x,a,d)-\omega(-x,a,d)\right] \\ & + \frac{4\left(1-\nu^2\right)(1+\alpha)\sigma_0 x}{\pi E\sqrt{d^2-x^2}}\left[\sin^{-1}\frac{a}{d}+\frac{\pi}{2}\frac{S-(1+\alpha)\sigma_0}{(1+\alpha)\sigma_0}\right] \end{aligned} \tag{71}$$

By letting $x_2 = \tau$, $t_2 = \eta$, $a_2 = \beta$, and $b_2 = \gamma$, equation 70 is reduced to a standard singular Cauchy integral equation

$$\int_\gamma^\beta \frac{\phi(\eta)}{\tau-\eta}d\eta = \pi\psi(\tau) \qquad \gamma < \tau < \beta \tag{72}$$

with

$$\phi(\eta) = \frac{\sigma_{con}(\eta)}{\sqrt{d^2-\eta}\sqrt{\eta}} \tag{73}$$

and

$$\psi(\tau) = \frac{E}{2\left(1-\nu^2\right)\sqrt{\tau}\sqrt{d^2-\tau}} H(\tau) \tag{74}$$

The solution to equation 72 can be obtained as

$$\phi(\tau) = \frac{1}{\pi}\sqrt{\frac{\beta-\tau}{\tau-\gamma}}\int_\gamma^\beta \sqrt{\frac{\eta-\gamma}{\beta-\eta}}\frac{\psi(\eta)}{\eta-\tau}d\eta \tag{75}$$

Considering the previous variables, after variable transformation, the solution can be rewritten as

$$\sigma_{con}(x) = \frac{Ex\sqrt{d^2-x^2}\sqrt{a^2-x^2}}{\pi\left(1-\nu^2\right)\sqrt{x^2-b^2}}\int_b^a \frac{\sqrt{t^2-b^2}}{\sqrt{d^2-t^2}\sqrt{a^2-t^2}}\frac{H(t)}{t^2-x^2}dt \tag{76}$$

Parameter b can be determined from the condition that contact stress at the end of the contact zone ($x = b$) is zero.

$$\int_b^a \frac{1}{\sqrt{d^2 - t^2}\sqrt{a^2 - t^2}} \frac{H(t)}{\sqrt{t^2 - b^2}} dt = 0 \tag{77}$$

Parameter d is obtained from the condition of the limitation in stresses at the end of the cyclic plastic zone ($x = d$).

$$\frac{\pi}{2}\left[S - (1+\alpha)\sigma_0\right] + (1+\alpha)\sigma_0 \sin^{-1}\frac{a}{d} - \int_b^a \frac{\sigma_{con}(t)}{\sqrt{d^2 - t^2}} dt = 0 \tag{78}$$

Combining equations 76-78, parameters b and d can be determined.

The model permits the determination of the crack opening stress S_{op}, which is defined at the external load $S = S_{op}$ at which crack surfaces are fully open, i.e., at the point where the process of active deformation of the material immediately ahead of the crack tip begins. The crack opening stress is calculated from the condition that the applied stress-intensity factor is equal to that caused by contact stresses on a closed part of the crack [24].

$$\left(S_{op} - S_{\min}\right)\sqrt{\pi a} = \frac{2\sqrt{a}}{\sqrt{\pi}}\left[\int_b^a \frac{\sigma_{con}(t)}{\sqrt{d^2 - t^2}} dt - \int_0^a \frac{\sigma^R}{\sqrt{d^2 - t^2}} dt\right] \tag{79}$$

The compressive residual stress will increase the crack open stress S_{op}. The effective stress range can be written as

$$\begin{aligned} \Delta S_{eff} &= S_{\max} - S_{op} \\ \Delta K_{eff} &= K_{\max} - K_{op} \end{aligned} \tag{80}$$

This model is appropriate for the growth of small fatigue cracks. By means of the plastic strip assumption, the model permits the estimation of the local stress-strain state at the crack tip and accounts for the presence of reverse plastic yielding, residual stresses, and the effects of plasticity-induced crack closure. However, this model involves singular integration that requires a careful treatment. This model is simpler than the strip model developed by Newman [29], which is embodied in the well-known FASTRAN model.

5.3 PLASTIC ZONE MODEL.

The effects of the shot-peen, cold-working process on crack growth can be considered to have the same effects as the overload: fundamentally, the residual stress field impedes the crack propagation. This model is based on the shape of the plastic zone.

The plastic strip models that were presented in the previous section are limited to the $\theta = 0$ crack plane. It is possible to estimate the extent of plasticity at all angles by applying an appropriate yield criterion. Consider the Von Mises equation.

$$\sigma_e = \frac{1}{\sqrt{2}}\left[(\sigma_1 - \sigma_2)^2 + (\sigma_1 - \sigma_3)^2 + (\sigma_2 - \sigma_3)^2\right]^{\frac{1}{2}} \tag{81}$$

where σ_e is the effective stress and σ_1, σ_2, and σ_3 are the three principal normal stresses. According to the von Mises criterion, yielding occurs when $\sigma_e = \sigma_y$, the uniaxial yield strength. For plane stress or plane strain conditions, the principal stresses can be written as

$$\sigma_1 = \frac{K_I}{\sqrt{2\pi r}}\cos\left(\frac{\theta}{2}\right)\left[1 + \sin\left(\frac{\theta}{2}\right)\right] \tag{82}$$

$$\sigma_2 = \frac{K_I}{\sqrt{2\pi r}}\cos\left(\frac{\theta}{2}\right)\left[1 - \sin\left(\frac{\theta}{2}\right)\right] \tag{83}$$

$$\sigma_3 = \begin{cases} 0 & \text{(plane stress)} \\ \dfrac{2vK_I}{\sqrt{2\pi r}}\cos\left(\dfrac{\theta}{2}\right) & \text{(plane stress)} \end{cases} \tag{84}$$

By substituting equations 82-84 into equation 81, setting $\sigma_e = \sigma_y$, and solving for r, estimates of the Mode I plastic zone radius as a function of θ are obtained.

$$r(\theta) = \frac{1}{4\pi}\left(\frac{K_I}{\sigma_y}\right)^2\left[1 + \cos\theta + \frac{3}{2}\sin^2\theta\right] \tag{85}$$

for plane stress, and

$$r(\theta) = \frac{1}{4\pi}\left(\frac{K_I}{\sigma_y}\right)^2\left[(1 - 2v)^2(1 + \cos\theta) + \frac{3}{2}\sin^2\theta\right] \tag{86}$$

for plane strain. Note the significant difference in the size and shape of the Mode I plastic zones for plane stress and plane strain. The latter condition suppresses yielding, resulting in a smaller plastic zone for a given K_I value.

Consider a structure subjected to a cyclic load with an overload, as shown in figure 47. After the application of the overload, the plastic zones formed at the crack tip as shown in figure 48 [30].

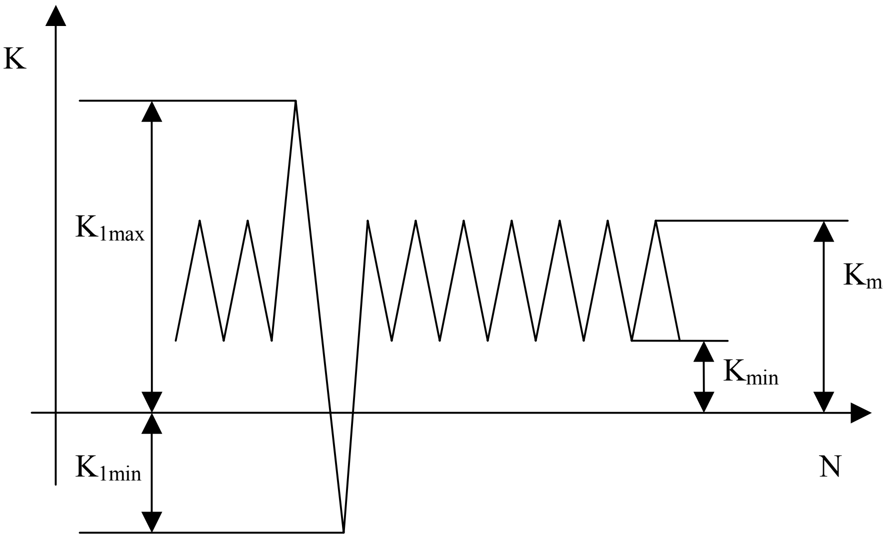

FIGURE 47. CONSTANT-AMPLITUDE CYCLIC LOAD WITH AN OVERLOAD

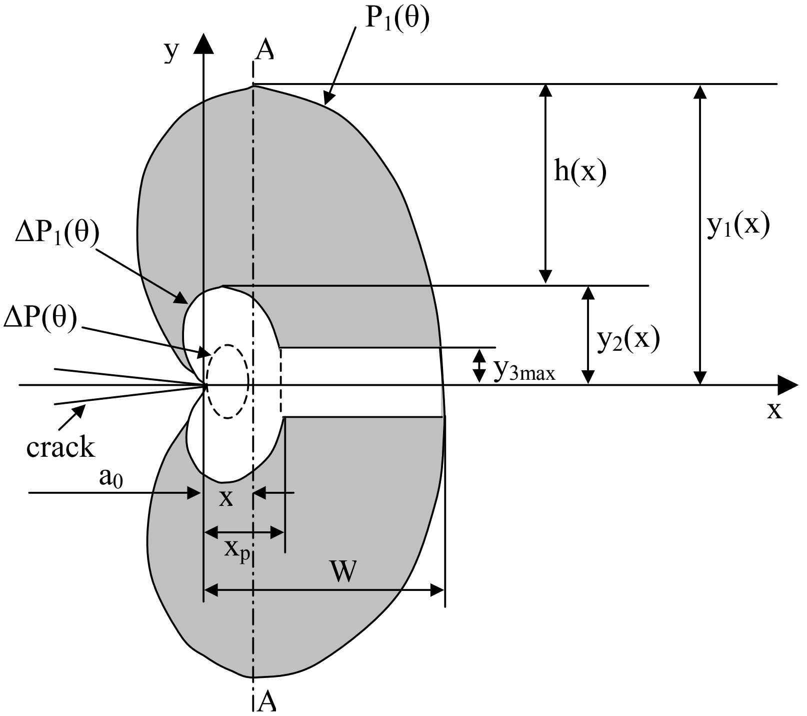
P$_1$(θ)
y
A
h(x)
y$_1$(x)
ΔP$_1$(θ)
ΔP(θ)
y$_2$(x)
y$_{3max}$
x
crack
a$_0$
x
x$_p$
W
A

FIGURE 48. PLASTIC ZONE FORMED AT THE CRACK TIP FOLLOWING AN OVERLOAD

The plastic zone of overload is

$$P_1(\theta) = \frac{1}{4\pi}\left(\frac{K_{1\max}}{\sigma_y}\right)^2 f(\theta) \tag{87}$$

The cyclic plastic zone of overload can be written as

$$\Delta P_1(\theta) = \frac{\beta}{4\pi}\left(\frac{(1-R_1)K_{1\max}}{2\sigma_y}\right)^2 f(\theta) \tag{88}$$

and the baseline cyclic plastic zone is

$$\Delta P\ (\theta) = \frac{\beta}{4\pi}\left(\frac{(1-R)K_{\max}}{2\sigma_y}\right)^2 f(\theta) \tag{89}$$

where

$$R_1 = \frac{K_{1\min}}{K_{1\max}} \tag{90}$$

β is the cyclic plastic zone size factor and depends on R. And from equations 85 and 86, it is obtained

$$f(\theta) = \left[1 + \cos\theta + \frac{3}{2}\sin^2\theta\right] \tag{91}$$

for plane stress and

$$f(\theta) = \left[(1-2v)^2(1+\cos\theta) + \frac{3}{2}\sin^2\theta\right] \tag{92}$$

for plane strain.

During the loading half cycle, the crack will only open when the load is great enough to make the CTOD equal to the compressive deformation during the unloading half cycle, i.e.,

$$CTOD = 2\delta,\ \delta = \lambda\Delta l \tag{93}$$

Δl is the stretch of the material element. For an element A-A just behind the crack tip, it can be calculated as

$$\Delta l = \int_{y_2}^{y_1} \varepsilon_p dy \tag{94}$$

Assuming that

$$\varepsilon_p = m\frac{\sigma_y}{E} \tag{95}$$

where *m* is a magnification factor depending on *x* and is assumed to be proportional to the height *h*(*x*) within the shade area.

$$m = m_0\frac{h(x)}{w} \tag{96}$$

where m_0 is a constant and *w* is the length of the overload-affected zone. From figure 48, it is noted that

$$\begin{aligned} h(x) &= y_1(x) - y_2(x) \quad \text{for } x < x_p \\ h(x) &= y_1(x) - y_{3\max}(x) \quad \text{for } x \geq x_p \end{aligned} \tag{97}$$

where

$$\begin{aligned} y_1(x) &= \frac{1}{4\pi}\left(\frac{K_{1\max}}{\sigma_y}\right)^2 \bar{y}_1(x) \\ y_2(x) &= \frac{\beta}{4\pi}\left(\frac{(1-R_1)K_{1\max}}{2\sigma_y}\right)^2 \bar{y}_2(x) \\ y_{3\max} &= \frac{\beta}{4\pi}\left(\frac{(1-R)K_{\max}}{2\sigma_y}\right)^2 \bar{y}_{\max} \end{aligned} \tag{98}$$

The crack tip opening displacement can be expressed as

$$CTOD = k\frac{K_{1\max}^2}{E\sigma_y} \tag{99}$$

and

$$\delta = \frac{\lambda m_0 \sigma_y}{Ew} h^2(x) \tag{100}$$

Employing the condition expressed by equation 93, the following equations for crack opening stress-intensity factor are derived.

$$\begin{aligned} K_{op}(x) &= M_0\left[\bar{y}_1(x) - \frac{\beta(1-R_1)^2}{4}\bar{y}_2(x)\right] R_m K_{\max} \quad \text{for } x < x_p \\ K_{op}(x) &= M_0\left[\bar{y}_1(x) - \frac{\beta(1-R)^2}{4R_m^2}\bar{y}_{\max}\right] R_m K_{\max} \quad \text{for } x \geq x_p \end{aligned} \tag{101}$$

where M_0 is an empirical material constant and

$$R_m = \frac{K_{1\max}}{K_{\max}} \tag{102}$$

Once the shape of the plastic zone is determined from a yield criterion, the crack opening load can be calculated from equation 101.

This model can be used to calculate the crack opening load for different cyclic loading patterns. By incorporating the effect of the residual stress (which can be thought of as an overload plastic zone), this model will be extended to consider the effect of the shot-peening process. The fact that significant differences in the size and shape of plastic zones for plane stress and plane strain will make this model very appropriate for modeling the 3D fatigue crack growth. For example, the material at the middle of the specimen is subject to plane strain conditions, while the material at the surface is subject to plane stress conditions. The plastic zone of the material experiencing plane strain is smaller than at the surface. According to this model, the effective stress intensity at the middle of the specimen will be greater than at the surface. Thus, the fatigue crack tunneling profile in the through crack will be conveniently simulated.

6. CONCLUSIONS.

The analytical model that was developed for shot peening is promising, and it will be developed further to take 200% coverage into account. Within reasonable accuracy, the experimentally observed effects were found in the present analytical model and very few numerical computations were necessary. In contrast, a complete numerical computation, such as finite element method, would have been extremely intensive, computationally inefficient, and entirely unrealistic. Therefore, the present analysis model appears to be a very suitable tool for commercial analyses. Based on the finite element, boundary element alternating method, AGILE 3D, and the modified NASGRO model were employed to simulate the effects of shot peening on the rotorcraft life enhancement. The numerical results obtained in this research showed that AGILE 3D is an accurate and efficient tool for predicting nonplanar three-dimensional (3D) fatigue crack growth in rotorcraft structural components. The results of validation of AGILE 3D for predicting 3D fatigue growth compared to the University of Washington test data are very good.

Moreover, the various fatigue crack growth models, including plastic strip model and plastic zone model, as discussed in section 5, in the presence of residual stresses and plasticity, will be developed further and incorporated into AGILE 3D to further validated against the test data. These models will be developed to other rotorcraft life enhancement methods, such as cold working, in the near future.

7. REFERENCES.

1. Khabou, M.T., Castex, L., and Inglebert, G., "The Effect of Material Behavior Law on the Theoretical Shot Peening Results," *Eur. J. Mech., A/Solids*, Vol. 9, pp. 537-549, 1990.

2. Li, J.K., Yao, M., Wang, D., and Wang, R., "Mechanical Approach to the Residual Stress Field Induced by Shot Peening," *Materials Sci. and Engineering*, A, Vol. 147, pp. 167-173, 1991.

3. Davis, R.M., "The Determination of Static and Dynamic Yield Stresses Using a Steel Ball," *Proc. Roc. Soc. A*, Vol. 197, p. 416, 1948.

4. Johnson, K.L., "Contact Mechanics," Cambridge University Press, 1985.

5. Schiffner, K. and Helling, C.D.G., "Simulation of Residual Stresses by Shot Peening," *Computers and Structures*, Vol. 72, pp. 329-340, 1999.

6. Deslaef, D., Rouhaud, E., and Rasouli-Yazdi, S., "3D Finite Element Models for Shot Peening Processes," *Materials Science Forum*, Vol. 347-349, pp. 241-246, 2000.

7. Meguid, S.A., Shagal, G., Stranart, J.C., and Daly, J., "Three-Dimensional Dynamic Finite Element Analysis of Shot-Peening Induced Residual Stresses," *Finite Elements in Analysis and Design*, Vol. 31, pp. 179-191, 1999.

8. Meguid, S.A., Shagal, G., and Stranart, J.C., "Finite Element Modeling of the Shot-Peening Residual Stresses," *Journal of Materials Processing Technology*, Vol. 92-93, pp. 401-404, 1999.

9. Al-Hassani, S.T.S., "Mechanical Aspects of Residual Stress Development in Shot Peening," ICSP1, Paris, 1981.

10. Zarka, J., Frelat, J., Inglebert, G., and Kasmai-Navidi, P., "A New Approach in Inelastic Analysis of Structures," CADLM, 1990.

11. Y.F. Al-Obaid, "Shot Peening Mechanics: Experimental and Theoretical Analysis," *Mech. Mater.*, Vol. 19, pp. 251-260, 1995.

12. Al-Hassani, S.T.S., "Shot Peening Mechanics and Structures," SAE paper, 821452, 1982.

13. Al-Hassani, S.T.S., “An Engineering Approach to Shot Peening Mechanics,” *Proc. of the second Int. Conf. on Shot Peening*, ICSP-2, Chicago, IL, 14-17 May 1984, H.O. Fuchs ed., Paramus, NJ: ASPS, p 275, 1984.

14. Guechichi, H., Castex, L., Frelat, L., Inglebert, G., “Predicting residual stress due to shot peening,” *Impact Surface Treatment*, (S.A. Meguid ed.), Elsevier, Applied Science Publishers LTD, 1986.

15. Mutoh, Y., Fair, G.H., Nobel, B., and Waterhouse, R.B., “The Effect of Residual Stresses Induced by Shot-Peening on Fatigue Crack Propagation in Two High Strength Aluminum Alloys,” *Fatigue Frac. Eng. Mater. Struc.*, Vol. 10, pp. 261-272, 1987.

16. Kopsov, I.E., “The Influence of Hammer Peening on Fatigue in High-Strength Steel,” *Int. J. Fatigue,* Vol. 13, pp. 479-482, 1991

17. De Los Rios, E.R., Walley, A., Milan, M.T., and Hammersley, G., “Fatigue Crack Initiation and Propagation on Shot-Peened Surfaces in A316 Stainless Steel,” *Int. J. Fatigue,* Vol. 17, pp. 493-499, 1995.

18. Farrahi, G.H., Lebrun, J.L., and Courtain, D., “Effect of Shot Peening on Residual Stress and Fatigue Life of a Spring Steel,” *Fatigue Frac. Eng. Mater. Struc.*, Vol. 18, pp. 211-220, 1995.

19. Zhu, X.Y. and Shaw, W.J.D., “Correlation of Fatigue Crack Growth Behavior With Crack Closure in Peened Specimens,” *Fatigue Frac. Eng. Mater. Struc.*, Vol. 18, pp. 811-820, 1995.

20. Hammonf, D.W. and Meguid, S.A., “Crack Propagation in the Presence of Shot-Peening Residual Stresses,” *Engineering Fracture Mechanics*, Vol. 37, pp. 373-387, 1990.

21. Song, P.S. and Wen, C.C., “Crack Closure and Crack Growth Behavior in Shot-Peened Fatigued Specimen,” *Eng. Frac. Mech*., Vol. 63, pp. 295-304, 1999.

22. Nakagaki, M. and Atluri, S.N., “Fatigue Crack Closure and Delay Effects Under Mode I Spectrum Loading: an Efficient Elastic-Plastic Analysis Procedure,” *Fatigue Frac. Eng. Mater. Struc*. Vol. 1, pp. 421-429, 1979.

23. Newman, J.C. Jr., “Finite-Element Analysis of Fatigue Crack Closure,” In *Mechanics of Crack Growth*, ASTM STP 590, ASTM, PA, pp. 281-301, 1976.

24. Panasyuk, V.V., Andreykiv, O.Y., Ritchie, R.O., and Darchuk, O.I., “Estimation of the Effect of Plasticity and Resulting Crack Closure During Small Fatigue Crack Growth,” *International Journal of Fracture*, Vol. 107, pp. 99-115, 2001.

25. De Los Rios, E.R., Trull, M., and Levers, A., “Modelling Fatigue Crack Growth in Shot-Peened Components of Al 2024-T351,” *Fatigue Fract. Engng Mater. Struct.*, Vol. 23, pp. 709-716, 2000.

26. Nikishkov, G.P., Park, J.H., and Atluri, S.N., "SGBEM-FEM Alternating Method for Analyzing 3D Non-Planar Cracks and Their Growth in Structural Components," *Computer Modeling in Engineering and Sciences*, Vol. 2, pp. 401-422, 2001.

27. Robertson, G.T., "The Effect of Shot Size on the Residual Stress Resulting From Shot Peening," *The Shot Peener*, Vol. 11, pp. 46-48, 1997.

28. Muskhelishvili, N.I., "Some Basic Problems of the Mathematical Theory of Elasticity," Nauka, Moscow, 707 pages, 1966.

29. Newman, J.C. Jr., "A Crack-Closure Model for Predicting Fatigue Crack Growth Under Aircraft Spectrum Loading," ASTM STP 748, ASTM, pp. 53-84, 1983.

30. He, Q.Z., "A Model for Calculating the Fatigue Crack Opening Load and Its Applications," *Fatigue Engng. Mater. Struct.*, Vol. **7**, pp. 41-53, 1984.

APPENDIX A—AGILE 3D'S CAPABILITIES IN FRACTURE MECHANICS ANALYSIS

Accurate calculation of the Mode I, II, and III stress-intensity factors for arbitrary three-dimensional (3D) surfaces and internal cracks continues to be one of the most pressing needs in field of applied fracture mechanics. Finite element and boundary element solutions have historically proven successful in analyzing cracks in finite bodies; however, disadvantages such as the requirement of a very fine mesh near the crack to capture the singularities associated with the crack tips remain necessary. The difficulties that are traditionally associated with mesh generation are compounded when fatigue crack growth analysis is considered, since intricate meshing and complicated matrix decomposition is required every time the crack size changes [A-1]. The associated high human labor costs and excessive computation time are considered to be the major drawbacks associated with the application of traditional finite element methods for the analysis of fracture mechanics problems.

A comprehensive software package (AGILE 3D) has been developed based on a highly efficient and accurate Symmetric Galerkin Boundary Element Method—Finite Element Method-based Alternating Method (SGBEM-FEAM) for the analysis of arbitrary nonplanar cracks in solid bodies. The finite element method (FEM) is used to perform stress analysis on a finite crackless body, while the SGBEM is used to perform stress analysis on the crack as if it were in an infinite body. The fracture mechanics solution is obtained through an iteration procedure, which alternates between the FEM and SGBEM solutions. The SGBEM is ideal for modeling cracks in infinite bodies, since the displacement discontinuity approach provides for simple modeling of the crack. Only one surface of the crack needs to be discretized, and the independence between the crack model and the finite element (FE) model allows simple modification of the crack model to simulate crack growth. A distinguishing feature of the inherent alternating method employed within AGILE 3D is that the FE model is completely decoupled from the boundary element (BE) model such that any and all restrictions on the mesh compatibility between the BE and FE models are alleviated.

AGILE 3D performs crack analysis by evaluating stress-intensity factors and predicting crack growth based on various fatigue models. These models determine the crack growth rate and direction under user-specified fatigue loading. AGILE 3D automatically updates the BE model of the 3D crack surface and regenerates the BE model as the crack advances, while the global FE model remains unchanged. The SGBEM-FEAM continually performs analysis on the updated, or grown, crack along the path determined by the fracture mechanics parameters. The life of the structural component is then estimated using either of the supported fatigue models: NASGRO, Walker, or Paris fatigue models. Since the BE and FE models are entirely independent, the user is not required to explicitly model the crack surface in the global or local meshes, ultimately allowing either model to be modified separately at any point during the analysis.

Alternating approaches, such as the Schwartz-Neumann alternating technique, have received much attention due to their stability, flexibility, accuracy, and efficiency in saving both computation and human labor time. The SGBEM-FEAM is a linear superposition method, which is a refinement of the Schwartz-Neumann alternating technique that has been developed over the years [A-1, A-2, and A-3]. The alternating method employed in AGILE 3D is used to obtain the fracture mechanics parameters such as the stress-intensity factors and the J-integral. This solution is found by iterating between the FE solution of an uncracked finite body and the BE solution of a crack in an infinite region. The cohesive tractions at the crack location in the uncracked finite element model and the residuals at the far-field boundaries of the analytical solution for the cracked infinite body are corrected through this iteration process.

The solution for the finite body with a crack is attained via the superposition principle of the FEM and SGBEM solutions. In an effort to compensate for the stresses caused by the presence of a crack, the FEM stresses at the location of the crack are used to solve the SGBEM problem of a crack in an infinite medium, which produces residual forces at the boundary of the FE model. This can be done with a direct procedure. However, the alternating method [A-1] provides a more efficient solution without assembling a joint SGBEM-FEAM matrix.

The SGBEM-FEAM approach defies typical BE or FE analysis restrictions since it avoids requiring that the models should be very detailed and contain aggressive mesh refinement near and around the crack tips. Since it is not required to define most of the mesh manually through a preprocessor, the FEAM method inherently eliminates many inaccuracies typically associated with human error. In summary, the efficient utilities within the FEAM code, allows the user to evaluate fracture parameters of cracks and their growth in a complicated structures accurately and efficiently.

The SGBEM-FEM alternating method is very suitable for modeling of fatigue crack growth. Since the BE and FE models are independent, only the BE model should be modified during crack growth modeling. The Paris, Walker, and NASGRO fatigue crack growth models are implemented into the AGILE 3D solver to express the functional relationship for crack growth rate through the range of the effective stress-intensity factor ΔK_{eff}.

For example, fracture mechanics analysis of a bulk 3D solid structure was performed using the SGBEM-FEAM solver implemented into the AGILE 3D software suite.

The global model, subject to the loading conditions, as shown in figure A-1, was created and analyzed using MSC.Patran/Nastran. An intermediate model was created from this global model and is distinguished by highlighted elements in figure A-2. When such a cracked complicated structure is to be analyzed, AGILE 3D easily solves for the fracture parameters via a series of multiple stages. After a conventional FE analysis of the entire structure is performed, a subregion of the structure surrounding the crack surface is modeled. Displacements and forces along the boundary of the subregion are then transferred from the data given in the original analysis. SGBEM-FEAM analysis is then performed on this smaller structure, which results in fracture parameters. The original FE model is not required to have intricately model the cracks and structural details, since the sole purpose of this analysis is to supply the appropriate boundary conditions for the SGBEM-FEAM stage of analysis. Therefore, this approach is computationally efficient and can be performed on a personal computer (PC) or a workstation. Utilities associated with this global-intermediate-local hierarchical approach were developed within AGILE 3D's graphical user interface module. These utilities link the AGILE 3D solvers with other commercial FE codes, such as NASTRAN and ANSYS, and provide the possibility of beginning the fracture mechanics analysis directly from existing FE results.

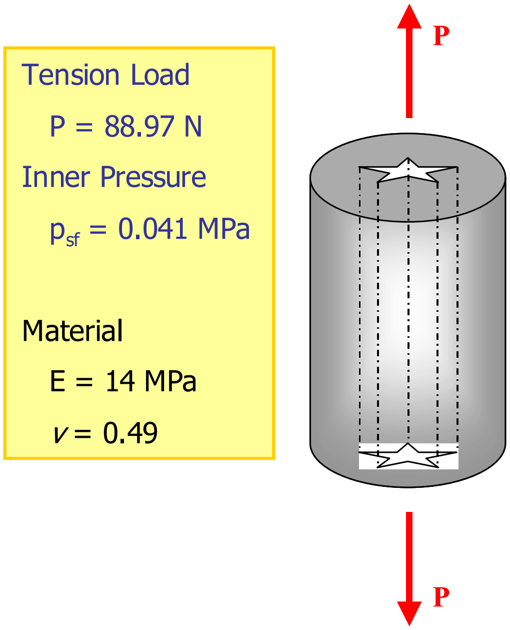
Tension Load
P = 88.97 N
Inner Pressure
p_{sf} = 0.041 MPa
Material
E = 14 MPa
ν = 0.49
P
P

FIGURE A-1. BULK SOLID STRUCTURE UNDER TENSION LOAD

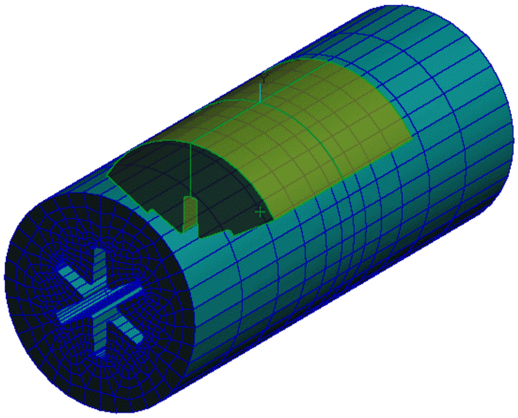

FIGURE A-2. GLOBAL AND INTERMEDIATE MODELS

A BE model of a semicircular crack (figure A-3) was modeled independent of the global and local FE mesh, hence, mesh compatibility between the BE and FE models is not required. This independence ultimately allows either model to be altered separately whenever necessary. However, an effort was made to ensure that the orientation and placement of the BE crack model was consistent with the global and local FE models, as shown in figure A-4.

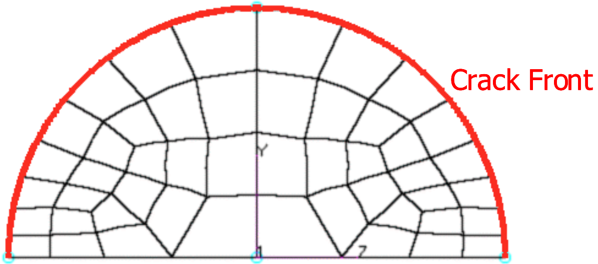

FIGURE A-3. BOUNDARY ELEMENT MODEL OF A SEMICIRCULAR CRACK

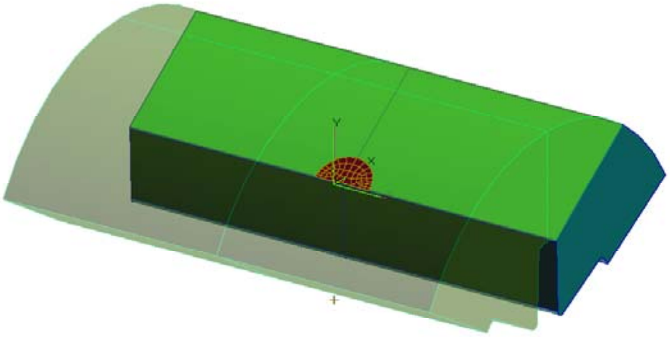

FIGURE A-4. JOINT BOUNDARY ELEMENT/FINITE ELEMENT MODEL DIAGRAM

Several fatigue models that are supported in the AGILE 3D solver are used to determine the crack growth rate and direction under user-specified fatigue loading. The BE model of the 3D crack surfaces is automatically updated and regenerated as the crack advances, while the FE model remains unchanged. The AGILE 3D solver continually performs fracture analysis on the updated, or grown, crack along the path determined by the fracture mechanics parameters. The life of the structural component is then estimated using either of the supported fatigue models: NASGRO, Walker, or Paris fatigue crack growth model. Figure A-5 presents the grown crack after a mere 5 minutes of analysis per increment. The computing time for 11 crack growth increments in the radial direction was a mere 3 hours using a laptop computer. Since the SGBEM-FEAM analysis is only performed on the local FE and BE models, this approach is computationally efficient and can accurately and efficiently be performed on a PC or a workstation.

In conclusion, AGILE 3D is an efficient and reliable code for the analysis of crack growth in finite bodies of complicated geometry and loading conditions. AGILE 3D is based on the Symmetric Galerkin Boundary Element Method-Finite Element Alternating Method for the fracture mechanics analysis of 3D nonplanar surface cracks. Three fatigue models were implemented into the package: Paris, Walker, and NASGRO fatigue crack growth models. Crack growth rates are calculated based on the *K* factor solutions to predict the location of the advanced crack front. The crack mesh is automatically updated to represent this crack front advancement. This process is automatically repeated through the entire crack growth process.

Ultimately, the life of the component is predicted based on crack growth as in damage tolerance approaches. Manpower cost can be dramatically reduced with AGILE 3D's independence of the FE and BE models as well as its automated crack growth features, which avoids mesh-regeneration all together.

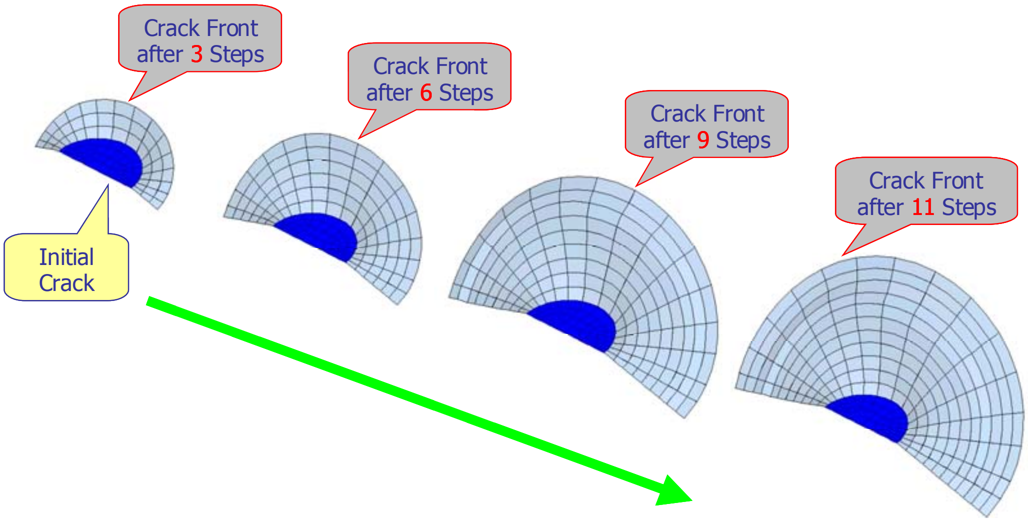
Crack Front after 3 Steps
Crack Front after 6 Steps
Crack Front after 9 Steps
Crack Front after 11 Steps
Initial Crack

FIGURE A-5. DEPICTION OF CRACK GROWTH

In this project, AGILE 3D was employed to validate the experimental data from the University of Washington.

REFERENCES.

A-1. Atluri, S.N., "Structural Integrity & Durability," *Tech Science Press*, 880 pages, 1997.

A-2. Atluri, S.N., "Computational Methods in the Mechanics of Fracture," Amsterdam North Holland, also translated into Russian, Mir Puhlishers, Moscow, 1986.

A-3. Atluri, S.N. and Nishioka, T., "On Some Recent Advances in Computational Methods in the Mechanics of Fracture," Plenary Lecture, Advances in Fracture Research, *Proceedings of the 7th International Conference on Fracture* (ICF7), Vol. 3, pp. 1923-1969, 1989.

APPENDIX B—EXPERIMENTS (UNIVERSITY OF WASHINGTON)

The life of a rotorcraft component under cyclic loading is governed by pre-existing small flaws that develop into observable cracks and eventually grow to a critical size, where brittle fracture occurs at N_f cycles of loading. For a given material and a set of cyclic loading conditions, this crack growth behavior is represented by the cyclic crack growth rate *da/dN* and the stress-intensity factor range, ΔK. The log-log plot of *da/dN* versus ΔK at a low crack growth rate starts with a steep slope with an appearance of a vertical asymptote that is referred to as the fatigue crack growth threshold. At a higher crack growth rate, the slope becomes steep again due to unstable crack growth just prior to final failure of the specimen. For the intermediate region of crack growth rate, *da/dN* is related to ΔK by Paris' law. Since a rotorcraft component is subjected to extremely high cycles of fatigue loading, the actual time to failure is relatively short after an observable crack is generated. Ideally, the allowable loading of a rotorcraft component should be such that ΔK is below the threshold stress-intensity factor, ΔK_{th}. For 7075-T7351 aluminum alloy, ΔK_{th} was shown to be less than 2 MPa√m [B-1].

While peening increases the fatigue life of steel components, peening of softer materials, such as high-strength aluminum, is found to be far more sensitive to the particular peening process. Work hardening due to shot peening has little influence on the fatigue behavior of aluminum, but compressive residual stress increased its fatigue life [B-2]. However, the visible surface damage and roughness induced by shot peening of high-strength aluminum can significantly decrease the fatigue life with the initiation of many fatigue cracks [B-3]. Careful polishing of the shot-peened surface without removing the residual compressive stress can restore and slightly increase the fatigue life [B-1]. Thus, an optimal combination of the shot peening and finishing processes of the peened surface is necessary for fatigue life improvement of high-strength aluminum.

This investigation did not generate ΔK_{th} data [B-4] due to the complex of the experimental protocol.

The objective of this section is to provide experimental data in support of the newly developed finite element code (AGILE 3D) for predicting fatigue crack growth in the presence of residual stress.

B.1 METHOD OF APPROACH.

Cyclic elastic-plastic stress-strain data with hysteresis and Baushinger's effect for a shot-peened 1.8-mm-thick 7075-T7351 plate was generated as part of the plane stress constitutive relation for the AGILE 3D code. The displacement field, which was determined by Moiré interferometry, at the crack tips of fatigued, shot-peened, double-edge-notched 7075-T7351 specimens was obtained for comparison with the University of California Irvine numerical data. Due to the relatively low fatigue loading, i.e., $\Delta K \approx 1 \sim 10$ MPa√m, used in this investigation, the plastic yield region is expected to be confined to about 1 mm from the crack tip with minor perturbation to the elastic strain and displacement fields generated by the fatigue load [B-5]. The resultant Moiré displacement field thus incorporates the influence of the residual compressive state, which is induced by shot peening, on the elastic displacement field of a loaded double-edged notch specimen.

A feasibility study of quantifying the effect of shot peening on *da/dN* by observing crack tunneling in severely shot-peened, thick, single-edged notch bend (SENB) was also undertaken. This study used the experienced gained in a stable crack growth study in 2024-T3 SENB specimens [B-6]. Cyclic elastic-plastic stress-strain data for as-received 8.1-mm-thick 2024-T3 plate and the crack growth profile in the fatigued 2024-T351 SENB specimens were recorded.

B.2 FATIGUE TESTS.

B.2.1 Specimens.

Tension/tension fatigue tests were conducted with thin 7075-T7351 aluminum alloy, double-edged notch (DEN) specimens. Limited three-point bend fatigue testing of 8.1-mm-thick 2024-T351 aluminum alloy SENB were also conducted.

The DEN specimens were machined from a 1.8-mm-thick 7075-T7351 aluminum stock plate and loaded parallel to the rolling direction. Subsized tensile coupons and the DEN fatigue specimens with 60° V- or straight notches are shown in figure B-1. The notch tips of the DEN specimens were chevron notched by a sharp razor blade. The SENB specimens, as shown in figure B-2, were machined from an 8.1-mm-thick 2024-T351 aluminum stock plate with a crack perpendicular to the rolling direction, i.e., in the L-T direction. These specimens were mildly or severely shot peened under the following conditions:

- Intensity 0.007A, shot size 230-280, coverage 1.0
- Intensity 0.017A, shot size 230-280, coverage 1.0

B.2.2 Testing Systems.

Uniaxial tension tests using the subsized tensile coupons and three-point bend fatigue testing with the SENB specimens were conducted in an Instron Model 8511 test system with a 13344-NT load cell. Due to the lack of compression grips for this test system, the compressive stress-strain relation was not obtained. The tension/tension fatigue test of the DEN specimens was conducted in a Sontag Universal Fatigue Testing Machine Model SF-01-U.

Crack length at various stages of crack growth in the DEN specimen were optically measured with a Shimadzu Micro-Hardness Tester microscope after removing the specimens from the loading frame. The crack in a SENB specimen, which was fractured after a given fatigue cycle, was recorded by a charge-coupled device camera to provide a digitized crack-tunneling profile.

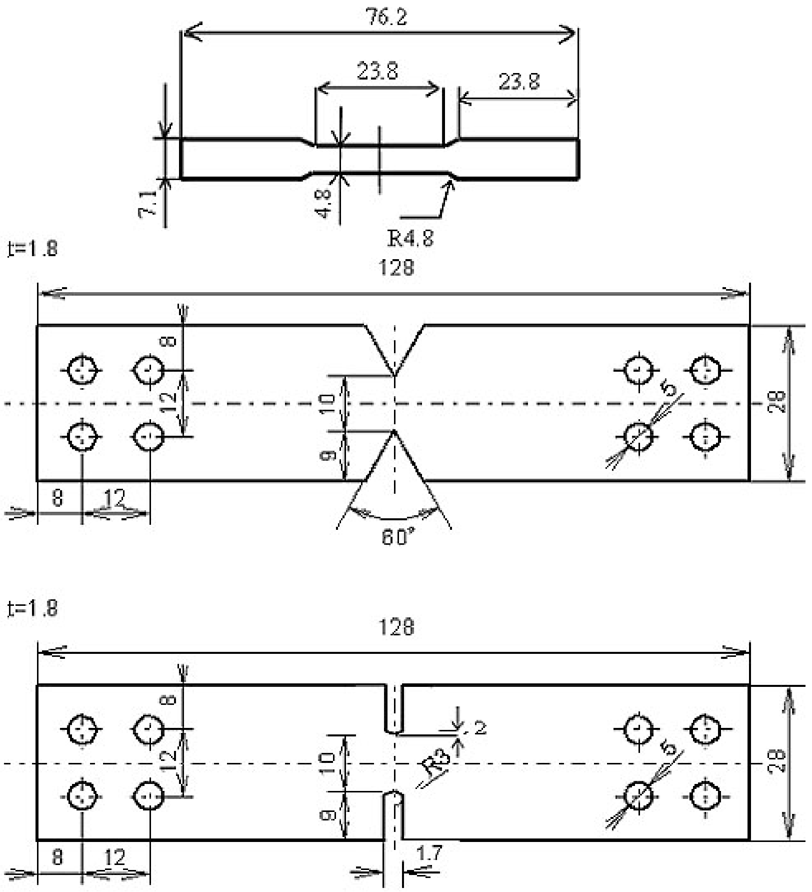
76.2
23.8
23.8
7.1
4.8
R4.8
t=1.8
128
8
12
10
9
5
28
8
12
60°
t=1.8
128
8
12
2
10
R3
9
5
28
8
12
1.7

All dimensions in mm

FIGURE B-1. SUBSIZE TENSILE SPECIMENS AND 60° V- AND STRAIGHT DOUBLE-NOTCHED SPECIMENS

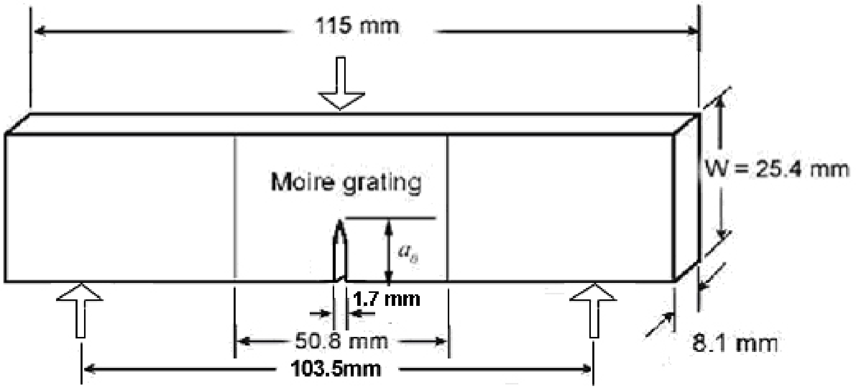
115 mm
Moire grating
a_0
W = 25.4 mm
1.7 mm
50.8 mm
103.5mm
8.1 mm

a_0 =13 mm

FIGURE B-2. SINGLE-EDGED NOTCH BEND SPECIMENS

The Moiré fringe pattern of a fatigued DEN specimen, which was loaded to its maximum fatigue load, $\sigma_{\max}$, in an Instron load frame, was recorded digitally in a Moiré interferometer bench, as shown in figure B-3. A specimen grating of 80 lines per mm that yields an accuracy of 0.012 mm per fringe was placed on the polished specimen surface. The Moiré fringes were then converted to in-plane displacements of the DEN specimen.

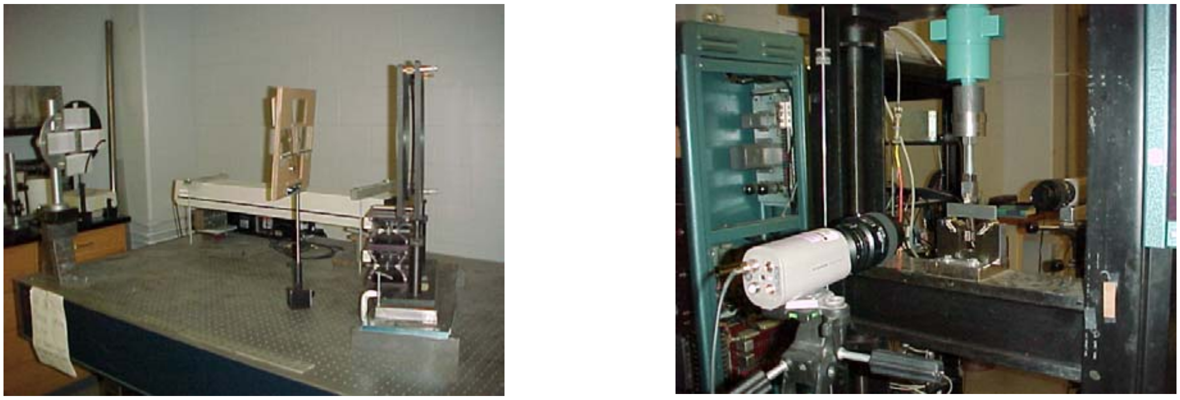

(a) Moiré bench with redirecting mirrors, mask, and collimating lens.

(b) Front view of specimen in load frame, and front camera.

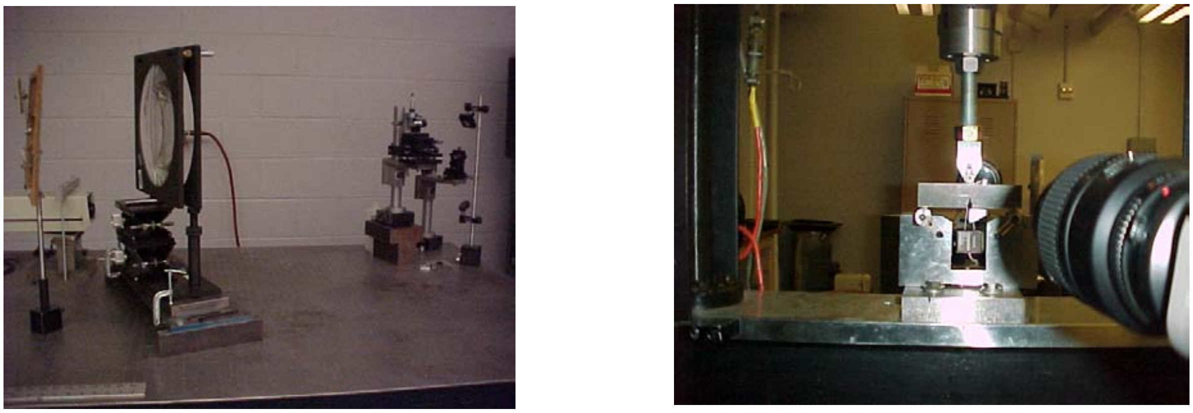

(c) Spatial filter assembly in front of collimating lens.

(d) Closeup view of specimen with CMOD gage attached.

FIGURE B-3. MOIRÉ INTERFEROMETRY BENCH

B.3 RESULTS.

Figures B-4 and B-5 show the uniaxial stress-strain data in the rolling direction of three mildly and two severely shot-peened 7075-T7351 subsize tension specimens of thickness t = 1.8 mm. A comparison of these curves with the corresponding curves of as-received 7075-T7351 shows that no significant difference exists between the as-received, mildly, and severely shot-peened 7075-T7361 aluminum of t = 1.8 mm. The results are virtually identical with the uniaxial stress-strain relation of the as-received 7075-T7351 subsize tension specimens.

In view of the above, the uniaxial tension stress-strain relation for the shot-peened thicker, i.e., t = 8.1 mm, 2024-T351 sheet was not sought. The uniaxial tension data of the as-received 2024-T351 sheet was deemed adequate for numerical modeling of the shot-peened 2024-T351 SENB specimens.

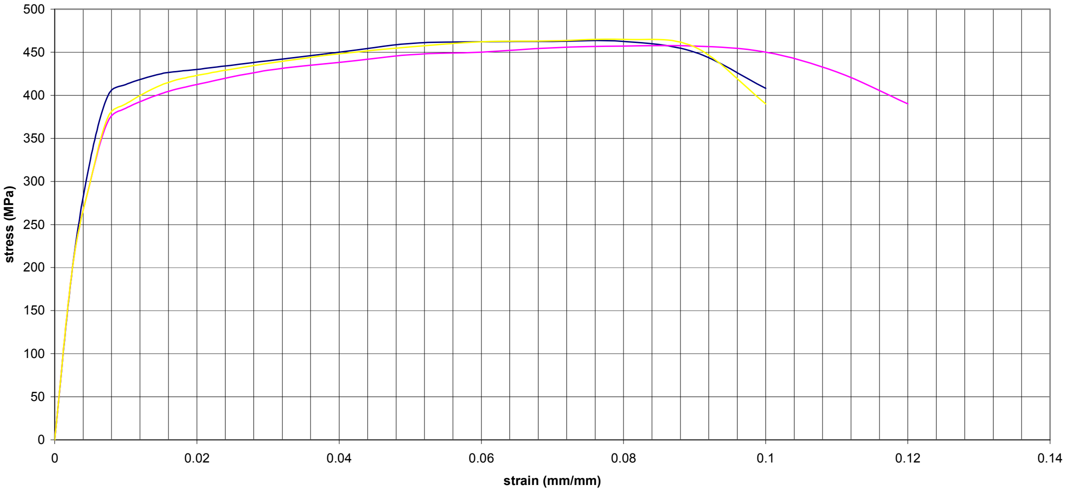

FIGURE B-4. UNIAXIAL TENSION TESTS IN THE ROLLING DIRECTION OF MILDLY SHOT-PEENED 7075-T351 SUBSIZE TENSILE SPECIMENS, t = 1.8 mm

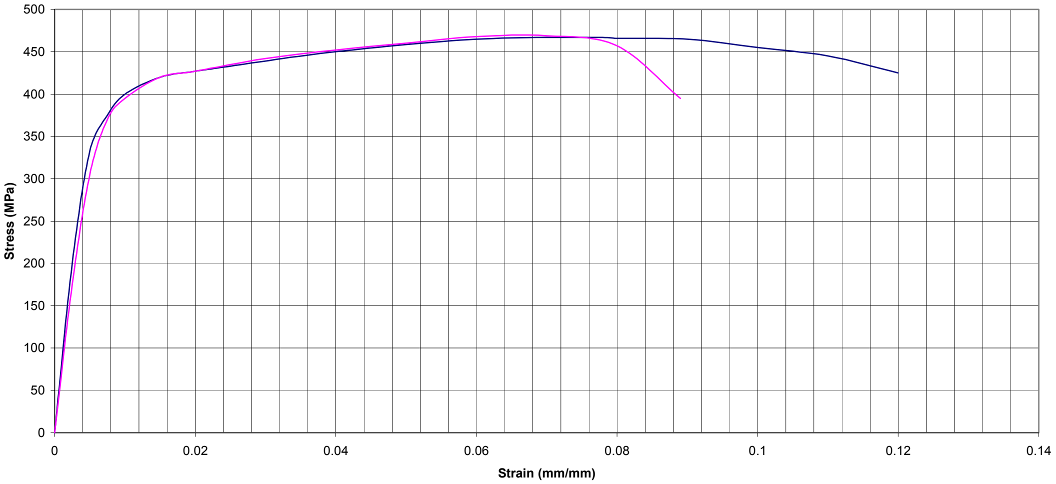

FIGURE B-5. UNIAXIAL TENSION TESTS IN THE ROLLING DIRECTION OF SEVERELY SHOT-PEENED 7075-T351 SUBSIZE TENSILE SPECIMENS, t = 1.8 mm

Seventeen shot-peened DEN test specimens were fatigued at 10 Hz at $R \approx 0$ and $\sigma_{max} \approx 7.0$, 14.8 and 35.3 MPa. Figures B-6 and B-7 show the *da/dN* versus ΔK data of the shot-peened 7075-T7351 DEN specimens with sharp and 60° V-notches. Eight of the severely shot-peened DENs were polished to a mirror-finished surface. Superimposed on these data points are the *da/dN* data generated by S. Forth [B-1] for 7075-T7351 CT specimens of 2.3 mm thickness. The *da/dN* data for the mildly shot-peened DEN specimens coincides with the National Aeronautics and Space

Administration (NASA) data. The *da/dN* data for the severely shot-peened DEN specimen also coincides with the NASA data at the higher drive force of Δ*K*. Near the threshold Δ*K*, the *da/dN* data of the severely shot-peened DEN specimen is slightly above the NASA data. Surface polishing of the severely shot-peened DEN shows a decided decrease in *da/dN* data relative to the unpolished severely shot-peened and mildly shot-peened DEN specimens and relative to the NASA data. Table B-1 shows the load, crack growth of Δ*a*, Δ*K*, and *da/dN* associated with the data points in figures B-6 and B-7.

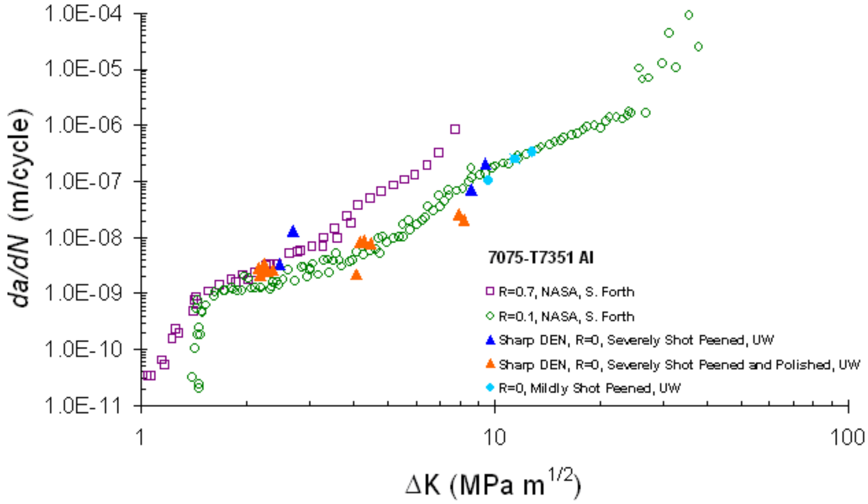

FIGURE B-6. *da/dN* VERSUS Δ*K* OF SHOT-PEENED 7075-T351 DEN SPECIMENS (SHARP NOTCH)

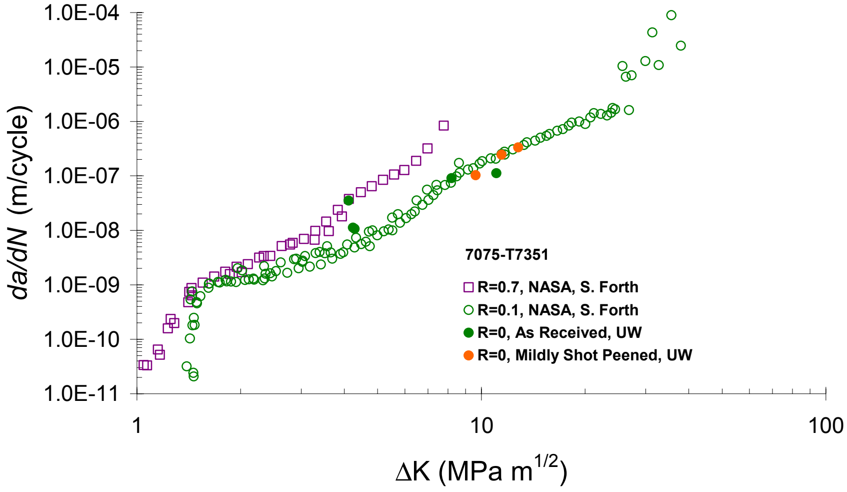

FIGURE B-7. *da/dN* VERSUS Δ*K* OF SHOT-PEENED 7075-T351 DEN SPECIMENS (60° NOTCH)

TABLE B-1. AVERAGE *da/dN* VERSUS AVERAGE Δ*K* OF SHOT-PEENED 7075-T7351 DEN SPECIMENS

	Nominal Stress (MPa)		Δ*K* (MPa√m)	*da/dN* (m/cycle)	Δ*a* (mm)
60° notch	35.3	Mildly Shot Peened	11.287	2.27E-07	2.45
Sharp Notch	8.83	Severely Shot Peened	2.584	8.18E-09	2.0613
		Severely Shot Peened and Polished	2.243	2.7E-09	1.249
	17.65	Severely Shot Peened and Polished	4.246	6.85E-09	0.846
	35.3	Severely Shot Peened	9.021	1.38E-07	1.233
		Severely Shot Peened and Polished	8.074	2.33E-08	0.443

Figure B-8 shows a Moiré fringe pattern in a shot-peened 7075-T7351 60° V-notched DEN specimen loaded at 35.3 MPa after 26,000 cycles of fatigue. Figure B-9 shows the corresponding average vertical (v-) displacement field in the vicinity of the 60° notch. Figure B-10 shows the interpolated vertical displacement in the vicinity of the 60° notch. Since the computed maximum plane stress, plastic zone size under monotonic loading is 0.18 mm, the difference with that of the as-received v-displacement field, represents the influence of the residual compressive stress induced by severe shot peening.

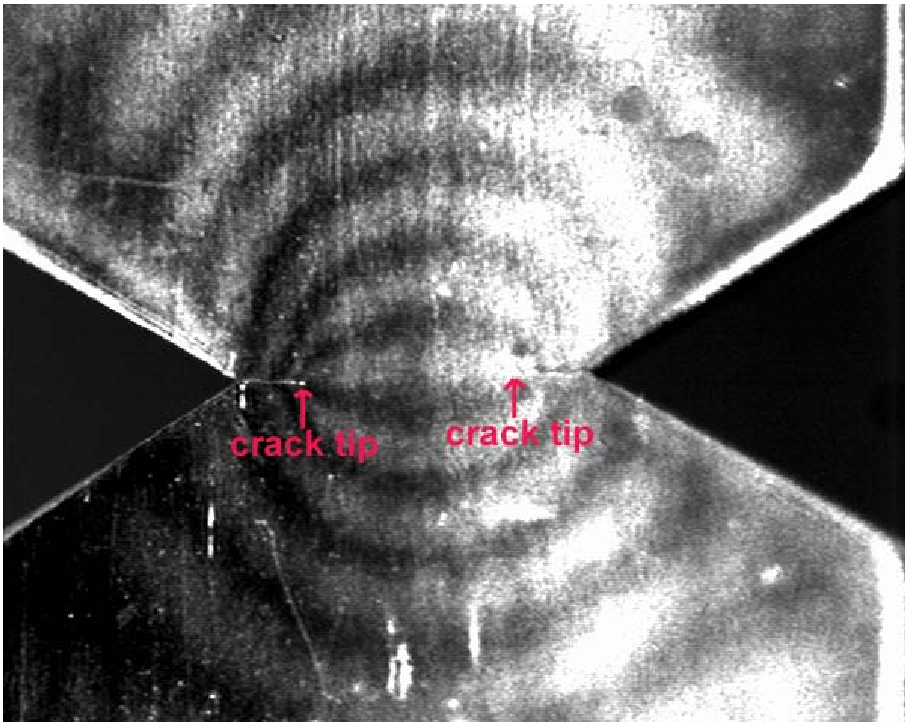

FIGURE B-8. MOIRÉ V- FIELD OF MILDLY SHOT-PEENED, 7075-T351 60° NOTCHED DEN SPECIMENS σ_{max} = 35.3 MPa, *N* = 31,000 CYCLES

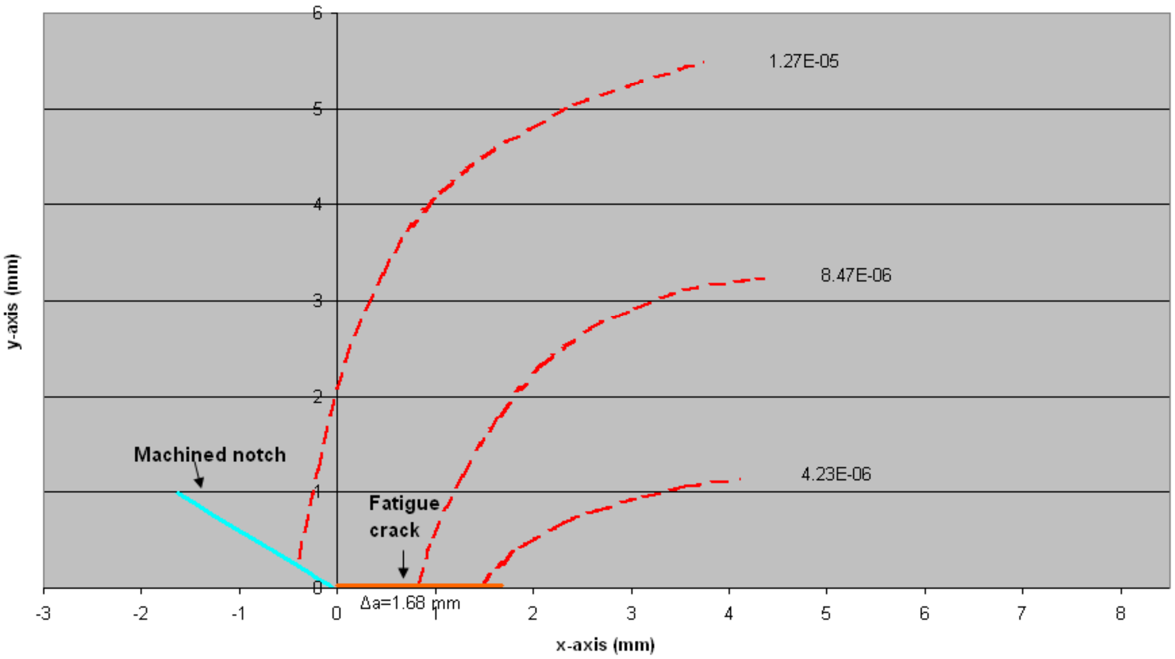

FIGURE B-9. V-DISPLACEMENT FIELD OF MILDLY SHOT-PEENED 7075-T351 60° NOTCHED DEN SPECIMENS σ_{max} = 35.3 MPa, N = 31,000 CYCLES

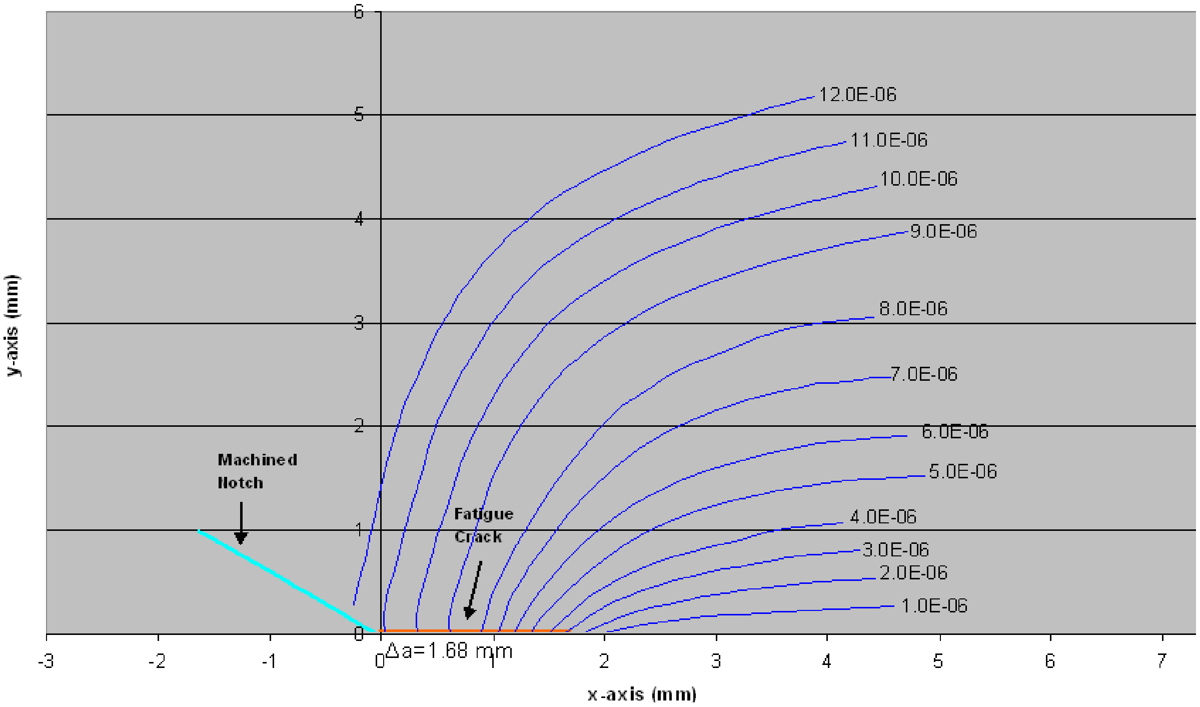

FIGURE B-10. INTERPOLATED V-DISPLACEMENT FIELD OF MILDLY SHOT-PEENED 7075-T351 60° NOTCHED DEN SPECIMENS σ_{max} = 35.3 MPa, N = 31,000 CYCLES

B.4 DISCUSSION.

The surface stress concentration at the rough surface texture of the mildly shot-peened 7075-T7351 DEN specimens offset the residual compressive stress generated by shot peening. The rougher surface of the severely shot-peened 7075-T7351 DEN specimens with larger stress concentration increased the crack growth rate. When this surface stress concentration was eliminated by polishing, a moderate decrease in crack growth rate was observed. While this trend is obvious, a quantitative assessment of the decrease in *da/dN* in the polished, severely shot-peened 7075-T7351 specimens will require a large volume of fatigue data.

The limited fatigue data of the 2024-T351 SENB specimen in table B-2, unpolished and polished, showed that severe shot peening increased the crack growth rate. The fatigue life of the as-received 2024-T351 SENB specimen was 10,392 cycles, that is, 59 percent higher than the average fatigue life of peened specimens. Apparently the local damage caused by severe shot peening persisted in spite of the polishing, which removed the surface roughness caused by the severe shot peening.

TABLE B-2. AVERAGE *da/dN* VERSUS AVERAGE ΔK OF SHOT-PEENED 7075-T7351 SENB SPECIMENS

Severely Shot Peened				
Test	ΔK (MPa√m)	*da/dN* (m/cycle)	Δa (m)	*N* (cycles)
C1	18.60	3.11E-06	2.03E-03	4965
C2 failure	38.71	2.61E-06	5.73E-03	7325
Severely Shot Peened and Polished				
D1 failure	36.65	2.97E-06	5.56E-03	6387
D2	18.38	3.07E-06	1.85E-03	4965
D3 failure	37.21	3.24E-06	5.67E-03	5894

B.5 REFERENCES.

B-1. Forth, S. C. and Favrow, K.W., "Experimental and Computational Investigation of Three-Dimensional Mixed-Mode Fatigue," *Fatigue Fract. Engng. Mater. Struct.*, Vol. 25, pp. 3-15, 2002.

B-2. Mutoh, Y., Fair, G.H., Nobel, B., and Waterhouse, R.B., "The Effect of Residual Stresses Induced by Shot-Peening on Fatigue Crack Propagation in Two High Strength Aluminum Alloys," *Fatigue Frac. Eng. Mater. Struc.*, Vol. 10, pp. 261-272, 1987.

B-3. Was, G.S., Pelloux, R.M., and Frabolot, M.C., "Effect of Shot Peening Methods on the Fatigue Behaviors of Alloy 7075-T6," First International Conference on Shot Peening, Paris, 14-17 September, 1981, Pergamon Press, pp. 445-451, 1981.

B-4. Annual Book of ASTM Standards, Vol. 03.01, No. E647, "Measurement of Fatigue Crack Growth Rates" and E1681 "Determination of a Threshold Stress Intensity Factor for Environment-Assisted Cracking of Metallic Material," ASTM 1997.

B-5. Nicoletto, Gianni, "Fatigue Crack Tip Strains in 7075-T6 Aluminum Alloy," *Fatigue & Fracture of Engineering Materials and Structures*, Vol. 10, No. 1, pp. 37-49, 1987.

B-6. Jackson, J.H., "A 3-Dimensional Experimental and Numerical Analysis of the T^*_ε Integral in Aluminum Fracture Specimens," A PhD dissertation submitted to the University of Washington, 2001.